https://doi.org/10.5194/egusphere-2026-6687
Preprint. Discussion started: 5 November 2026
© Author(s) 2026. CC BY 4.0 License.

What reflectance reveals about particle scattering in bio-optical models across contrasting Mediterranean waters

Eva Álvarez[1,4], Guido Occhipinti[2], Gianpiero Cossarini[1], Fabrizio Bernardi Aubry[3], Federica Braga[3], Paolo Lazzari[1]

[1]National Institute of Oceanography and Applied Geophysics – OGS, Trieste, 34010, Italy

[2]MARBEC (IRD, Ifremer, CNRS, Univ Montpellier), Sète Cedex, 34203, France

[3]Institute of Marine Science – National Research Council of Italy (CNR–ISMAR), Venezia, 30122, Italy

[4]Instituto Español de Oceanografía (IEO–CSIC), Centro Oceanográfico de Gijón/Xixón, 33212, Spain

Correspondence to: Eva Álvarez (eva.alvarez@ieo.csic.es) and Paolo Lazzari (plazzari@ogs.it)

Abstract. Spectral ocean-colour reflectance is increasingly used to constrain marine ecosystem models, yet its potential to provide direct observational constraints on process-based biogeochemical models remains underexplored. Here we calibrate multi-wavelength remote sensing reflectance ($R_{RS}(\lambda)$) using a genetic algorithm within a one-dimensional configuration of the Biogeochemical Flux Model. The approach is applied to two contrasting Mediterranean environments: an open-ocean ecosystem in the Ligurian Sea (BOUSSOLE observatory) and an optically complex coastal site in the Northern Adriatic Sea (Acqua Alta oceanographic tower - AAOT). At both sites, the calibration successfully reproduces observed $R_{RS}(\lambda)$ at six visible wavelengths, demonstrating that the model captures the main features of the $R_{RS}(\lambda)$ spectra across contrasting trophic regimes. However, the mechanisms used by the model to match $R_{RS}(\lambda)$ differ markedly and reveal distinct controls on particle scattering. At BOUSSOLE, $R_{RS}(\lambda)$ calibration primarily adjusts phytoplankton and small-particle optical properties, improving phytoplankton biomass estimates and increasing particulate backscattering. This highlights the dominant role of small and algal particles in shaping backscattering in oligotrophic waters. In contrast, at AAOT, $R_{RS}(\lambda)$ calibration mainly modifies suspended particulate matter (SPM) optical parameters, with limited changes in the biogeochemical state. Overall, $R_{RS}(\lambda)$ calibration reproduces observed optical signals while revealing site-dependent controls on particulate backscattering. Sensitivity and calibration exercises improved predictive capability within the calibrated parameter space, but residual error patterns revealed potential structural limitations or simplifications in the model's optical representation. This work demonstrates the potential of $R_{RS}(\lambda)$ observables to guide improvements in the representation of particle optical properties and biogeochemical processes in marine ecosystem models.

https://doi.org/10.5194/egusphere-2026-6687
Preprint. Discussion started: 5 November 2026
© Author(s) 2026. CC BY 4.0 License.

1 Introduction

The component of the radiation field that is scattered upward and re-emerges from the ocean is expressed as reflectance or remote-sensing reflectance ($R_{RS}(\lambda)$), an essential quantity to interpreting satellite ocean color data (IOCCG, 2020). The magnitude and spectral shape of $R_{RS}(\lambda)$ are primarily determined by the absorption ($a(\lambda)$) and backscattering ($b_b(\lambda)$) (known as inherent optical properties, IOPs) of seawater optical constituents, including phytoplankton, coloured dissolved organic matter (CDOM), non-algal particles (NAP) and pure seawater (Stramski et al., 2004; Zaneveld, 1995). Through absorption and scattering processes, these constituents control the attenuation and spectral redistribution of light at different wavelengths in the water column, allowing $R_{RS}(\lambda)$ spectra to be used to infer information about the composition of water bodies (e.g., Gregg and Casey, 2009; Lee et al., 2002; O'Reilly et al., 1998).

The spectral signal of $R_{RS}(\lambda)$ results from coupled absorption and scattering processes that are not uniquely attributable to individual components. Variability in the optical properties of non-algal substances can produce distinct $R_{RS}(\lambda)$ spectra even for similar phytoplankton biomass and size structure, leading to the well-known non-uniqueness of the $R_{RS}(\lambda)$–biogeochemistry relationship (IOCCG, 2020). Non-algal constituents exhibit strong spatial and temporal variability for a given chlorophyll (Chl) concentration (Babin et al., 2003b; Organelli et al., 2014). While CDOM and phytoplankton absorption largely shape $R_{RS}(\lambda)$ in open-ocean waters, light scattered by suspended particles often becomes the dominant control on $R_{RS}(\lambda)$ variability in coastal waters (Babin et al., 2003a). Consequently, changes in $R_{RS}(\lambda)$ driven by mineral particles, detritus and/or CDOM may be misinterpreted as changes in phytoplankton biomass, highlighting the difficulty of disentangling optical signals from multiple constituents.

These differences in the composition and relative contribution of optically active constituents have motivated the development of region- and water-type-specific R_{RS}-Chl relationships. In relatively clear waters, phytoplankton and associated optically active substances tend to covary, and phytoplankton-related processes generally account for a large fraction of the variability in the water-column IOPs. These waters are commonly referred to as Case-1 waters (Morel, 1988; Morel and Prieur, 1977). In contrast, in optically complex waters, non-algal constituents such as mineral particles and CDOM may vary independently of phytoplankton and contribute substantially to light absorption and scattering. These waters are commonly referred to as Case-2 waters (IOCCG, 2020). Consequently, the relationship between $R_{RS}(\lambda)$ and phytoplankton biomass is less direct in optically complex waters, where the observed spectral signal reflects the combined contributions of multiple constituents. Bio-optical algorithms developed for a specific water type may therefore not adequately represent the full range of optical conditions encountered across different marine environments (e.g. from coastal to open sea) (IOCCG, 2000; Morel and Prieur, 1977).

Forward radiative-transfer models (RTMs), which simulate $R_{RS}(\lambda)$ from the IOPs of the water column, provide a framework to link biogeochemical state variables with ocean-colour observations. By explicitly representing the absorption and scattering contributions of clear water, phytoplankton, CDOM and/or suspended particles, RTMs can translate changes in the biogeochemical state into their corresponding optical signatures (Baird et al., 2016; Dutkiewicz et al., 2015; Gregg and

https://doi.org/10.5194/egusphere-2026-6687
Preprint. Discussion started: 5 November 2026
© Author(s) 2026. CC BY 4.0 License.

Rousseaux, 2017). Coupling process-based biogeochemical models with spectrally resolved RTMs therefore creates an opportunity to use $R_{RS}(\lambda)$ not only as a model output, but also as a direct observational constraint on the underlying biogeochemical state (Jones et al., 2016; Lazzari et al., 2024). However, the information that can be extracted from $R_{RS}(\lambda)$ depends strongly on the optical regime and on the degree of overlap between the spectral signatures of different constituents. Because similar changes in $R_{RS}(\lambda)$ may arise from substantially different combinations of biogeochemical constituents, the ability of a coupled model to represent the optical properties of diverse water types is critical for effectively transferring information from observations to the biogeochemical state. This requires (1) radiative-transfer formulations capable of representing the relevant optical regimes and (2) approaches that can exploit spectral observations to constrain the coupled optical–biogeochemical system. Assessing how effectively information contained in $R_{RS}(\lambda)$ can be transferred to modelled biogeochemical variables across contrasting optical environments is therefore an important step towards a more direct integration of ocean-colour observations into marine ecosystem modelling.

Regional seas provide a valuable testbed for evaluating coupled optical–biogeochemical models because they encompass a broad range of optical and biogeochemical conditions within a relatively constrained geographical domain. The Mediterranean Sea is particularly well suited for this purpose, spanning clear, oligotrophic open waters where phytoplankton and CDOM largely determine the optical properties (Morel and Gentili, 2009), as well as productive and coastal environments where suspended mineral and detrital particles can contribute substantially to the observed optical signal (Babin et al., 2003b; Zibordi and Berthon, 2024). Indeed, the Mediterranean regional ocean-colour products commonly distinguish between open and optically complex coastal waters using different bio-optical approaches (MedOC4, (Volpe et al., 2019) and AD4, (Berthon and Zibordi, 2004) and merge them according to the water type present (Mélin and Vantrepotte, 2015; Volpe et al., 2019). This diversity provides an opportunity to test whether the information contained in spectral $R_{RS}(\lambda)$ can be transferred consistently to biogeochemical variables across contrasting optical regimes, and to identify where the assumptions linking optical properties to ecosystem state become limiting.

Coupling radiative-transfer models to BGC/ecosystem models to link simulated biogeochemical components with the resulting $R_{RS}(\lambda)$ is increasingly being implemented within the operational Copernicus Marine Service (CMS) BGC models suite (Cossarini et al., 2025; Grégoire et al., 2026; Macé et al., 2025; Terzić et al., 2021). Since simplified or imperfect RTMs can introduce systematic mismatches between simulated and observed optical properties, particularly in optically complex basins such as the Mediterranean Sea, regional modelling operational chains have increasingly focused on refining the representation of the optical components of these models (Coppini et al., 2023). Such developments include the incorporation of additional optically active constituents (Lazzari et al., 2021b), or including greater diversity among existing functional groups (e.g., pigment types, Álvarez et al., (2022)). Despite these advances, most operational data-assimilation systems still assimilate derived products (e.g., Chl, productivity indices, or IOPs) rather than the full observed $R_{RS}(\lambda)$ spectrum. Direct spectrum-level assimilation of $R_{RS}(\lambda)$ is an emerging research direction (Lazzari et al., 2024; Soto López et al., 2025), but is not yet widely implemented in operational regional forecasting systems.

https://doi.org/10.5194/egusphere-2026-6687
Preprint. Discussion started: 5 November 2026
© Author(s) 2026. CC BY 4.0 License.

The overall aim of this study is to clarify how satellite-observed $R_{RS}(\lambda)$ spectra constrain coupled process-based optical–biogeochemical models, using the Biogeochemical Flux Model (BFM) framework for the Mediterranean Sea as a test case. Specifically, we aim (1) to identify the model parameters that exert the strongest influence on simulated $R_{RS}(\lambda)$ and assess whether they coincide with those controlling phytoplankton biomass (Chl and/or carbon) in the surface ocean, and (2) to evaluate the extent to which integrating observed $R_{RS}(\lambda)$ in BGC/ecosystem models improves the inference of phytoplankton community properties and the broader optical environment. To achieve this objective, we conducted a comprehensive sensitivity analysis (Sect. 3.1) followed by parameter calibration (Sect. 3.2) using two contrasting Mediterranean sites: the BOUSSOLE mooring, representative of open-ocean conditions, and the AAOT site in the northern Adriatic Sea, characterized by optically complex waters. An independent validation analysis then demonstrates the improvements achieved by the automatically optimized model (Sect. 3.3 and 3.4). Finally, starting from the optimized model, a set of targeted manual simulations are performed to test additional hypotheses and investigate the mechanisms responsible for the discrepancies that persisted after calibration (Sect. 3.5).

https://doi.org/10.5194/egusphere-2026-6687
Preprint. Discussion started: 5 November 2026
© Author(s) 2026. CC BY 4.0 License.

2 Methods

2.1 The sites

The characteristics of the two test sites used in this study are summarize in **Table 1**.

2.1.1 The BOUSSOLE observatory

The *Bouée pour l'acquisition de Séries Optiques à Long Terme* (BOUSSOLE) observatory is located in the Ligurian Sea, about 32 nautical miles off the coast of Nice, in the center of the anti-clockwise circulation of the Ligurian Sea where the water depth varies between 2350 and 2500 m, the currents are extremely low and terrestrial inputs are negligible (43.37°N, 7.90°E, **Fig. 1a**). The site is characterized by uniform optical properties and relatively low concentrations of optically active constituents, such as Chl and CDOM. Chl and CDOM are the main optical constituents and although their drivers are different, they tend to covary (Organelli et al., 2014; Pérez et al., 2016; Xing et al., 2014). Given the small contribution of non-algal particles in the site, living cells are the main scattering component. Thus, the site exemplifies the so-called Case 1 waters. The BOUSSOLE site is visited monthly by oceanographic cruises to collect optical and biogeochemical variables (Golbol et al., 2000). Only BGC field measurements are used in the present study.

2.1.2 The Acqua Alta Oceanographic Tower

The *Acqua Alta* Oceanographic Tower (AAOT) is installed about 8 miles off the coast of Venice, in the Northern Adriatic Sea, in a stretch of sea having a depth of about 19 m where it receives inputs of nutrients, sediments, and organic matter from terrestrial sources (45.31°N, 12.51°E, **Fig. 1b**). The site is subject to complex hydrodynamic processes including anti-clockwise circulation and the influence of winds that affect circulation patterns and water exchange between the open sea and the coastal area. Several major rivers, including the Po River, flow into the Northern Adriatic, contributing freshwater, sediment, and nutrients to the sea. Therefore, although these relatively nutrient-rich waters promote the growth of phytoplankton, there is an important presence of non-algal constituents of terrestrial and/or sea-floor/benthic origin that do not necessarily covary with Chl. The site exemplifies the so-called Case 2 waters. The AAOT is equipped with radiometric sensors and infrastructure for real-time data transfer, which contributes to the NASA AERONET-OC monitoring network (Zibordi et al., 2009). It is also an important fixed point for periodic acquisition of water column samples and analysis of biological and chemical parameters, which is done monthly. The AAOT contributes, among others, to the Long Term Ecological Research (LTER) Network.

https://doi.org/10.5194/egusphere-2026-6687
Preprint. Discussion started: 5 November 2026
© Author(s) 2026. CC BY 4.0 License.

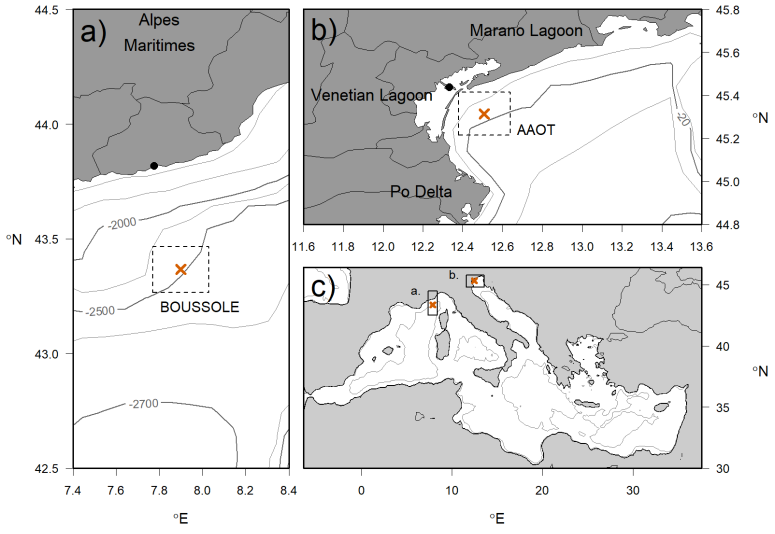


Figure 1: Map of the study sites at a) BOUSSOLE and b) AAOT, located in c) the Ligurian and Northern Adriatic Sea, respectively, of the Mediterranean Sea. The red crosses in a) and b) mark the position of the buoy and the tower respectively, and the dashed line boxes around them show the 20x20 km area averaged from remote sensing products.

140

Table 1: Summary of main aspects regarding the test sites, in terms of their location, the OC-based observations and the BGC and optical field-observations used in the present study, and the characteristics of the model simulations performed. SA and GA indicate the periods related to Sensitivity Analysis and to the Genetic Algorithm optimization, respectively.

	BOUSSOLE	**AAOT**
Characteristics		
Location (ºN, ºE)	43.37, 7.90	45.31, 12.51
Depth (m)	2448	19
Distance from coast (nm)	32	8
Class water type	Case I	Case II
OC-based observations		
Variables used	$R_{RS}(\lambda)$, $b_{bp}(443)$, Chl, phyto C	$R_{RS}(\lambda)$, $b_{bp}(443)$, Chl
Temporal coverage	2003-2020 (2017- for OLCI)	2003-2022 (2017- for OLCI)
Frequency of observations	daily (8-daily for phyto C)	daily
Field-based observations		
Variables used	Chl	Chl, phyto C, $b_{bp}(442)$, $b_{bp}(676)$
Temporal coverage	2002-2020	2011-2022 (-2016 for b_{bp})
Frequency of observations	monthly	monthly
Model simulations		
n model parameters	248	254
n depth layers	196	44
SA period	2012 W(J-M) & S(J-S)	2012 W(J-M) & S(J-S)
GA period	2013-2016	2010-2013
Validation period	2017-2020	2014-2017
Frequency of output	daily	daily

https://doi.org/10.5194/egusphere-2026-6687
Preprint. Discussion started: 5 November 2026
© Author(s) 2026. CC BY 4.0 License.

2.2 The observations

2.2.1 OC-based

The sources and procedures to obtain satellite $R_{RS}(\lambda)$ and ocean-colour (OC-) derived observations through the CMS were common for both sites (see Data Availability for sources). For all OC-based observations, in order to get timeseries at the test sites, the values in a 20x20km box around the sites (dashed line rectangles in **Fig. 1a-b**) were averaged as long as there were at least a 20% of non-NA values coverage.

$R_{RS}(\lambda)$, $b_{bp}(443)$ and Chl concentration were obtained for the period 2003 to 2022 at daily resolution from the CMS Mediterranean Sea L3 product: OCEANCOLOUR_MED_BGC_L3_MY_009_143 (E.U. Copernicus Marine Service Information, 2025). From the ´Reflectance, multi-sensor´ dataset we got $R_{RS}(\lambda)$ at 412, 443, 490, 510, 555 and 670 nm at 1km spatial resolution and from the ´Reflectance, OLCI´ dataset, we got $R_{RS}(\lambda)$ at 400, 412.5, 442.5, 490, 510, 560, 620, 665, 673.75, 681.25, 708.75, 778.75 and 865nm, at 300m spatial resolution. The 6 bands of the multi-sensor dataset (MULTI) were used for calibration and validation, whereas the 13 bands of the OLCI dataset (OLCI) that start in 2017 were only used for validation. From the ´Optics, multi-sensor´ dataset, we got the particle backscattering coefficient at 443 nm, only used for validation. $b_{bp}(443)$ is obtained via the QAAv6 model (Lee et al., 2002). From the ´Plankton, multi-sensor´ dataset, we got phytoplankton Chl concentration, only used for validation. Chl is obtained via region-specific merged algorithms (Case 1 waters: Volpe et al. (2019); Case 2 waters, Berthon and Zibordi (2004)).

Additionally, and only at BOUSSOLE, phytoplankton carbon was obtained from the Carbon-based Productivity Model (CbPM, Westberry et al., 2008) where phytoplankton carbon biomass is assessed from particulate backscattering coefficients ($b_{bp}(\lambda)$). In this study, we employed the 8-daily, 1/12º MODIS and VIIRS based estimates for the period 2017 to 2020 (see Data Availability for sources).

2.2.2 Field-based

The sources and procedures to obtain in situ biogeochemical and optical observations were site specific.

BOUSSOLE has been sampled monthly since approximately 2002 (Antoine and Vellucci, 2024). Seawater is generally collected at 12 discrete depths within the 0-400 m water column with 12-L Niskin bottles, from which water samples are collected to measure phytoplankton pigment concentrations through high-performance liquid chromatography (HPLC) analyses following the procedure fully described in (Ras et al., 2008), from which we used total Chl concentrations.

AAOT has been sampled monthly since 2011 through a standardized multidisciplinary protocol. At each visit, discrete water samples are collected from the surface and the bottom for subsequent analysis of phytoplankton biomass and Chl. Total Chl was estimated from 200 ml of water filtered at low vacuum pressure onto Whatman GF-F filters on board; filters were kept at –20°C until they were analysed in the laboratory. Chl concentrations were determined fluorometrically (Holm-Hansen et al., 1965) in 90% acetone extracts with a Turner Trilogy Laboratory Fluorometer. Phytoplankton samples were preserved in

https://doi.org/10.5194/egusphere-2026-6687
Preprint. Discussion started: 5 November 2026
© Author(s) 2026. CC BY 4.0 License.

formalin neutralized with hexamethylenetetramine (4 % final concentration), nano- and microphytoplankton were settled in 5–25 ml chambers for 12–24 h and later identified and quantified using an inverted microscope (Utermöhl, 1958; Zingone et al., 2010). To estimate the phytoplankton carbon content, the biovolume of the phytoplankton cells was first calculated by fitting the cell shapes to geometric models (Hillebrand et al., 1999); then the carbon content was obtained from the average biovolumes for each species using the conversion formulas proposed by Menden-Deuer and Lessard (2000).

Additionally, and only at AAOT, we considered optical data measured in the field. The CoAST-BioMAP dataset (Zibordi and Berthon, 2024) collects timeseries of near- surface marine optical properties at the AAOT fixed coastal site. In the present study, we considered the optical backscattering coefficient at 442 and 476 nm (bb442 and bb676 in the dataset) reported for AAOT from 2014 to 2016, and use it for validation.

2.3 The Biogeochemical Flux model (GOTM-BFM)

The Biogeochemical Flux Model (BFM) is a mechanistic marine ecosystem model designed to represent the cycling and interactions of key biogeochemical elements and the dynamics of marine planktonic ecosystems (Vichi et al., 2007). BFM was coupled to the General Ocean Turbulence Model (GOTM) through the Framework for Aquatic Biogeochemical Models (FABM; Bruggeman and Bolding, 2014), which provides a flexible framework for coupling biogeochemical models and ecosystem modules to hydrodynamic models. In this study, this coupling was used to configure BFM in one-dimensional (1D) water-column setups. GOTM (Burchard et al., 1999) is a 1D water-column model that resolves the vertical dynamics of salinity, temperature, and turbulence, thereby providing the physical environment driving the biogeochemical processes simulated by BFM at each study site.

The version of BFM used in this study comprises 54 state variables. These include inorganic nutrients, represented by nitrate nitrogen ($N^{(3)}$), ammonium ($N^{(4)}$), phosphorus ($N^{(1)}$) and silica ($N^{(5)}$), dissolved oxygen ($O^{(2)}$), four phytoplankton types ($P^{(1)}$ to $P^{(4)}$), four types of grazers ($Z^{(3)}$ to $Z^{(6)}$) and heterotrophic bacteria ($B^{(1)}$). Organic matter is represented by three pools of non-coloured ($R^{(1)}$ to $R^{(3)}$) and corresponding coloured ($X^{(1)}$ to $X^{(3)}$) dissolved organic matter (CDOM) and non-living particulate organic matter ($R^{(6)}$). The carbonate system is resolved through dissolved inorganic carbon ($C^{(3)}$) and total alkalinity. The formulation and differential equations governing the temporal evolution of these state variables are described in detail in the BFM documentation (Vichi et al., 2020) and previous applications of the model (e.g., Lazzari et al., (2012) and are, therefore, not reproduced here.

Within FABM, the biogeochemical model is coupled to a spectrally resolved light module (light_spectral, LS hereafter), which calculates the propagation of light through the water column across 33 wavebands centred between 250 and 3700 nm, with a spectral resolution of 25 nm within the visible range (Lazzari et al., 2021a; Terzić et al., 2021). This propagation is determined by the wavelength-dependent absorption, scattering, and backscattering properties of the modelled constituents. The total absorption by phytoplankton ($a_{PH}(\lambda)$, m^{-1}) is the sum of the products of PFTs Chl ($P^{(1\text{ to }4)}{}_{Chl}$, mg Chl m^{-3}), the Chl-

https://doi.org/10.5194/egusphere-2026-6687
Preprint. Discussion started: 5 November 2026
© Author(s) 2026. CC BY 4.0 License.

specific absorption spectrum ($a_{PH}^{*(i)}$, m^2 mg Chl^{-1}), equal to those used in Álvarez et al. (2023), and a scaling factor that allows the mean absorption cross-section from 387.5 to 800 nm to match the value defined by the parameter epsPi:

$$a_{PH}(\lambda) = \sum_{i=1,2,3,4} a^{*(i)}_{PH}(\lambda) \cdot P^{(i)}_{Chl-a} \cdot epsPi / \int_{387.5}^{800} a^{*(i)}_{PH}(\lambda)\ d\lambda / (800 - 387.5)\,, \quad (1)$$

The total scattering by phytoplankton ($b_{PH}(\lambda)$, m^{-1}) was assumed to be function of phytoplankton biomass and it was calculated as the sum of the products of phytoplankton C ($P^{(1\text{ to }4)}_C$, mg C m^{-3}), the C-specific scattering spectrum ($b_{PH}^{*(i)}$, m^2 mg C^{-1}), equal to those used in Álvarez et al. (2023), and a scaling factor that allows the mean scattering cross-section from 387.5 to 800 nm to match the value defined by the parameter bpsPi:

$$b_{PH}(\lambda) = \sum_{i=1,2,3,4} b^{*(i)}_{PH}(\lambda) \cdot P^{(i)}_{C} \cdot bpsPi / \int_{387.5}^{800} b^{*(i)}_{PH}(\lambda)\ d\lambda / (800 - 387.5)\,, \quad (2)$$

The absorption of detritus ($a_{NAP}(\lambda)$, m^{-1}) is modelled as an exponential function which decreases with increasing λ, where the reference absorption at 440 nm is calculated as the product of the carbon component of detritus ($R^{(6)}_C$, mg C m^{-3}) and their mass-specific absorption coefficients at 440 nm (aparcoeff, m^2 mg C^{-1}) and Sapar is the spectral slope of the detritus absorption coefficients between 350 and 500 nm (nm^{-1}) that governs the decline with λ, as follows:

$$a_{NAP}(\lambda) = aparcoeff \cdot R^{(6)}_C \cdot exp[-Sapar \times (\lambda - 440)]\,, \quad (3)$$

The scattering by detritus ($b_{NAP}(\lambda)$, m^{-1}) is computed as an exponential function of λ, where the reference scattering at 550 nm is calculated as the product of $R^{(6)}_C$ and the mass-specific scattering coefficient at 550 nm (bparcoeff, m^2 mg C^{-1}), and Sbpar is the exponent the governs the rate of exponential decline with λ, as follows:

$$b_{NAP}(\lambda) = bparcoeff \cdot R^{(6)}_C \cdot (550/\lambda)^{Sbpar}\,, \quad (4)$$

The total absorption by CDOM ($a_{CDOM}(\lambda)$, m^{-1}) is the sum of the products of the carbon component of each CDOM lability ($X^{(1\text{ to }3)}_C$, mg C m^{-3}) and their mass-specific absorption coefficients at 450 nm (Xicoeff, m^2 mg C^{-1}), where SdomXi is the spectral slope of the CDOM absorption coefficients between 350 and 500 nm (nm^{-1}) that governs the decreasing absorption with increasing λ, as follows:

$$a_{CDOM}(\lambda) = \sum_{i=1,2,3} Xicoeff \cdot X^{(i)}_C \cdot exp[-SdomXi \cdot (\lambda - 450)]\,. \quad (5)$$

2.3.1 Vertical discretization

The 1D configuration of GOTM-BFM for the BOUSSOLE site consists of a water column of 2448 m, subdivided in 196 vertical levels, and for the AAOT site consists of a water column of 18.9 m, subdivided in 44 vertical levels. In both cases, the grid has higher resolution at surface and the bottom, and has been generated using the iGOTM toolweb (https://igotm.bolding-bruggeman.com/, accessed 12/10/2021).

https://doi.org/10.5194/egusphere-2026-6687
Preprint. Discussion started: 5 November 2026
© Author(s) 2026. CC BY 4.0 License.

2.3.2 Atmospheric forcing

Atmospheric forcing was prescribed for the period 1995-2022 using hourly fields from the ECMWF ERA5 reanalysis, including 10m zonal and meridional wind components, sea-level pressure, 2m air temperature and dew point humidity, and precipitation. Atmospheric pCO_2 was prescribed as a constant value of 400 ppm throughout the simulations. Spectrally resolved plane downwelling irradiance (W m^{-2}) at sea surface was obtained in two streams, direct ($E_{d0}(\lambda)$) and diffuse ($E_{s0}(\lambda)$) at 15-min intervals from the OASIM model extracted at the coordinates of each study site (Lazzari et al., 2021a).

2.3.3 The bottom

The bottom boundary was treated differently for the two study sites. For the BOUSSOLE setup, the water column was considered effectively infinite, and no benthic remineralisation or return fluxes were prescribed. In the AAOT setup, the BenthicLayer module was activated to represent the first-order remineralisation and return of organic matter sinking below 16.9 m. Organic carbon, phosphorus, and nitrogen were returned to the water column as $C^{(3)}$, $N^{(1)}$ and dissolved inorganic nitrogen (DIN), with remineralisation timescales set by the parameters TauC, TauP, and TauN, respectively (**Table A1**). The returned DIN was partitioned between nitrate ($N^{(3)}$) and ammonium ($N^{(4)}$) in a proportion defined by the parameter Amm_rem (**Table A1**). For the optical component, the bottom boundary was not considered at either site, and therefore no bottom reflection or attenuation of downwelling irradiance was prescribed.

2.3.4 Lateral conditions at AAOT

Since BMF does not account for SPM dynamically, we provided SPM concentrations at AAOT as a lateral condition. Daily fields of OC-based estimates of non-algal SPM were obtained from the Ifremer ftp server (ftp://ftp.ifremer.fr/ifremer/cersat/products/gridded/ocean-color/atlantic/EUR-L4-SPIM-ATL-v01/). This product is processed by the OC5 algorithm (Gohin et al., 2005) that merges data from SeaWiFS, MODIS, MERIS and VIIRS satellite sensors and estimates the load of non-algal SPM. The algorithm has been validated against in situ coastal observations for the English Channel, Bay of Biscay and north-western Mediterranean Sea (Gohin, 2011). Starting 2020, Sentinel-2/HR provides an SPM product for coastal waters of the Mediterranean basin. We observed a good match between SPM concentrations for the period Sentinel-2/HR and Ifremer/OC5 overlap (data not shown), we chose the latter for the time coverage.

Timeseries of SPM concentration (g m^{-3}) were extracted in a 0.1x0.1 degree box around the AAOT, smoothed with a Savitzky-Golay filter and passed to the optical component of BFM as an extra term in the light equations, assuming that the concentration is the same throughout the water column. SPM absorption was estimated with an exponential dependency on λ (Gallegos et al., 2011), where spmc1 allows for the possibility of some absorption at long wavelengths, spmc2 scales the absorption at the reference wavelength (440 nm), and spmS governs the rate of exponential decline with λ:

https://doi.org/10.5194/egusphere-2026-6687
Preprint. Discussion started: 5 November 2026
© Author(s) 2026. CC BY 4.0 License.

$$a_{SPM}(\lambda) = (spmc1 + spmc2 \cdot exp[-spmS \cdot (\lambda - 440)]) \cdot SPM \quad (6)$$

SPM scattering ($b_{SPM}(\lambda)$) and backscattering ($b_{bSPM}(\lambda)$) were computed by multiplying SPM concentration by the non-wavelength dependent parameters spmb and spmbb (m^2 g^{-1}), respectively (Woźniak et al., 2018). As consequence, the AAOT setup has five more parameters than the BOUSSOLE setup.

2.3.5 Initialization

Weekly vertical profiles of T/S and BGC variables ($N^{(1)}$, $N^{(3)}$, $N^{(5)}$, $O^{(2)}$, $C^{(3)}$, and total alkalinity) were obtained from the CMS reanalysis (Cossarini et al., 2021) for BOUSSOLE and from the CADEAU North Adriatic model (Bruschi et al., 2021) for AAOT. The profiles are linearly interpolated onto the model vertical grid and used for initialization. T/S profiles were constrained by a monthly nudging and biogeochemistry by a yearly nudging. Since BGC variables were required for nudging, the GOTM-BFM simulations only did cover the periods available in the CMS reanalysis (1999-2022) and the CADEAU North Adriatic model (2006-2017), respectively. All other variables were set to constant values throughout the water column. The initial values of $R^{(1)}$, $R^{(2)}$ and $R^{(3)}$ were 80, 400 and 480 mg C m^{-3}, respectively. The initial values of $X^{(1)}$, $X^{(2)}$ and $X^{(3)}$) were 1, 3 and 1.25 mg C m^{-3}, respectively. All PFTs were initialized to 8 mg C m^{-3} and 0.16 mg Chl m^{-3}. Bacteria, zooplankton and $R^{(6)}$ were all initialized to 1 mg C m^{-3}.

2.3.6 Spectrally resolved light transmission and computation of the observable $R_{RS}(\lambda)$

The radiative-transfer scheme explicitly resolves the propagation of light through the water column and computes the upwelling light field and the radiance emerging from the water surface, thereby enabling the direct simulation of the observable $R_{RS}(\lambda)$. At each wavelength, total absorption ($a(\lambda)$), scattering ($b(\lambda)$) and backscattering ($b_b(\lambda)$) of the water column are determined from the additive contributions of seawater and the IOP_S of constituents represented in the model, as:

$$a(\lambda) = a_W(\lambda) + a_{PH}(\lambda) + a_{NAP}(\lambda) + a_{CDOM}(\lambda) + a_{SPM}(\lambda)\,, \quad (7)$$

$$b(\lambda) = b_W(\lambda) + b_{PH}(\lambda) + b_{NAP}(\lambda) + b_{SPM}(\lambda)\,, \quad (8)$$

$$b_b(\lambda) = b_W(\lambda) \cdot br_W + \sum_{i=1,2,3,4} b_{PH}^{(i)} \cdot bbrPi + b_{NAP}(\lambda) \cdot bb_to_b + bb_{SPM}(\lambda)\,, \quad (9)$$

where $a(\lambda)$ results from the absorption by water molecules ($a_W(\lambda)$, m^{-1}), phytoplankton ($a_{PH}(\lambda)$, m^{-1}, Eq. 1), R6 ($a_{NAP}(\lambda)$, m^{-1}, Eq. 3), CDOM ($a_{CDOM}(\lambda)$, m^{-1}, Eq. 5), and SPM ($a_{SPM}(\lambda)$, m^{-1}, Eq. 6); $b(\lambda)$ and $b_b(\lambda)$ result from the scattering and backscattering, respectively, by water ($b_W(\lambda)$, m^{-1}**)**, phytoplankton ($b_{PH}(\lambda)$, m^{-1}, Eq. 2), $R^{(6)}$ ($b_{NAP}(\lambda)$, m^{-1}, Eq. 4) and SPM ($b_{SPM}(\lambda)$, m^{-1}). We did not consider any wavelength dependency on the $b(\lambda)$ to $b_b(\lambda)$ ratio for any of the constituents: for water, NAP and phytoplankton, their $b_b(\lambda)$ was computed as their respective $b(\lambda)$ times a constant backscattering to total scattering ratio (0.05 for water (Morel, 1974), bb_to_b for $R^{(6)}$ and bbrPi for $P^{(1\ to\ 4)}$), and for SPM, $b_{bSPM}(\lambda)$ was computed by

https://doi.org/10.5194/egusphere-2026-6687
Preprint. Discussion started: 5 November 2026
© Author(s) 2026. CC BY 4.0 License.

multiplying SPM concentration by the non-wavelength dependent parameter spmbb (**Table A1**). The total backscattering by particles, $b_{bp}(\lambda)$, is computed equally to $b_b(\lambda)$ (Eq. 9) excluding the contribution of water.

The vertical propagation of spectrally resolved light is then computed using a three-stream radiative-transfer formulation (Aas, 1987; Ackleson et al., 1994; Gregg, 2002), which resolves the downward irradiance, scalar irradiance, and upwelling irradiance as a function of depth. Rather than reproducing the full set of differential equations that can be consulted in previous BFM setups (Álvarez et al., 2022, 2023; Lazzari et al., 2024), we describe the resulting optical pathway: incident spectral irradiance at the sea surface ($E_{d0}(\lambda)$ and $E_{s0}(\lambda)$) is propagated through the water column in two streams, $E_d(\lambda)$ and $E_s(\lambda)$, according to the depth- and wavelength-dependent absorption and scattering properties, while the upwelling light field, $E_u(\lambda)$, results from the redistribution of photons by scattering. The resulting upwelling radiance is used to calculate the subsurface irradiance reflectance, $R_0(\lambda)$, as the dimensionless ratio between the upwelling radiance at the water surface ($E_u^{TOP}(\lambda)$) in the most superficial layer (k=1) relative to the incoming irradiance just below ocean surface as follows:

$$R_0(\lambda) = E_u^{TOP}(\lambda)[k = 1]/(E_{d0}(\lambda) + E_{d0}(\lambda)) \,, \tag{10}$$

In order to compare to the reflectance seen by satellites, $R_0(\lambda)$ is converted during post-processing to subsurface remote sensing reflectance, $R_{RS}(\lambda,0^-)$, using the bidirectional function Q (Eq. 11), that varies seasonally between 3.59 and 4.57 at BOUSSOLE and between 3.61 and 4.63 at AAOT. Lastly, $R_{RS}(\lambda,0^-)$ is converted to above surface remote sensing reflectance, $R_{RS}(\lambda,0^+)$, with the conversion by Lee et al. (2002):

$$R_{RS}(\lambda, 0^-) = R_0(\lambda)/Q \,, \tag{11}$$

$$R_{RS}(\lambda, 0^+) = \left(0.52 \cdot R_{RS}(\lambda, 0^-)\right)/\left(1 - 1.7 \cdot R_{RS}(\lambda, 0^-)\right) \,, \tag{12}$$

Hereafter, we refer to this quantity as $R_{RS}(\lambda)$ that has units of sr^{-1}.

https://doi.org/10.5194/egusphere-2026-6687
Preprint. Discussion started: 5 November 2026
© Author(s) 2026. CC BY 4.0 License.

2.4 The tool: Parallel sensitivity analysis and calibration (ParSAC)

ParSAC is a tool written in Python to perform sensitivity analysis and automatic optimization of a selected set of model parameters in a coupled physical-biogeochemical simulation (Bruggeman and Bolding, 2020) and constitutes a built-in functionality of the FABM configuration of BFM. In this study, we used ParSAC within the coupled GOTM–BFM framework to identify the parameters exerting the strongest control on simulated $R_{RS}(\lambda)$, surface Chl and phytoplankton carbon at the two sites. Based on the sensitivity results, the most influential parameters were subsequently calibrated, with satellite-derived $R_{RS}(\lambda)$ as observational constraint.

2.4.1 Sensitivity analysis (SA)

ParSAC builds its sensitivity analysis workflow upon the Sensitivity Analysis Library in Python (SALib, Usher et al. (2016)) to systematically perturb model input parameters and quantify their influence on model outputs (Saltelli et al., 2007). To assess the relative importance of the biogeochemical parameters at each study site, all parameters were perturbed simultaneously, comprising 248 parameters for BOUSSOLE and 254 for AAOT, the latter including six additional parameters controlling the interaction between SPM and light. Parameter values were varied within a range of ±30% around their respective reference values (**Table A1**). The parameter space was sampled to generate an ensemble of parameter vectors comprising 20 realizations per input parameter, resulting in 4900 and 5080 parameter sets for BOUSSOLE and AAOT, respectively.

The sensitivity analysis was conducted for two representative three-month periods: winter (JFM) and summer (JAS). For each period, all simulations were initialized from common initial conditions obtained from a spin-up simulation using the reference parameter values that last 2 years for the winter analysis and 2.5 years for the summer analysis.

Sensitivity was evaluated for three types of model output: i) $R_0(\lambda)$ from 250 to 800 nm in 25 nm steps, ii) Chl and iii) total phytoplankton carbon concentrations averaged in the first 10 m of the water column. For each output variable, ParSAC estimates a multiple linear regression model relating output variability to the perturbations of the input parameters. The standardized regression coefficients (βi) were used as global sensitivity indices, with their magnitude indicating the relative contribution of each parameter to the variability of the corresponding model output. In addition, ParSAC provides the coefficient of determination, R^2, representing the fraction of the model-output variance explained by the multiple linear regression. Based on the sensitivity analysis, the parameters were ranked according to their absolute standardized regression coefficient ($|\beta i|$) for each target output.

2.4.2 Automatic optimization (GA)

We selected for calibration the ten most influential parameters based on their average $|\beta i|$ across all target outputs, together with the most influential parameter for each individual output, which resulted in 12 parameters for each test site. In this work, ParSAC bases the calibration workflow on the Differential Evolution method (Storn and Price, 1997), a genetic

https://doi.org/10.5194/egusphere-2026-6687
Preprint. Discussion started: 5 November 2026
© Author(s) 2026. CC BY 4.0 License.

algorithm (GA) that iteratively explores the parameter space and seeks the set of parameter values that minimizes the mismatch between model results and observations, or equivalently maximizes the likelihood of the observations given the model predictions.

The population size (1 generation) was set to a minimum of 10 times the number of parameters included in the optimization. Parameter bounds were user-defined (**Table 2** and **Table 3**, Appendix B Figs. **B8** and **B9**), and the initial population was generated by sampling the parameter space within these bounds. Each individual simulation covered a four-year period, preceded by a two-year spin-up. Consequently, only observations prior to the 4-years validation period, from 2013 to 2016 at BOUSSOLE and from 2010 to 2013 at AAOT, were considered in the calibration procedure.

The cost function was based exclusively on subsurface irradiance reflectance, $R_0(\lambda)$, at the six wavelengths provided by the MULTI-sensor CMS product: $R_0(412)$, $R_0(443)$, $R_0(490)$, $R_0(510)$, $R_0(555)$, $R_0(670)$. To ensure comparability of satellite observations and model output, the modelled spectral bands were linearly interpolated to the satellite wavelengths and the satellite observations, which are provided as $R_{RS}(\lambda, 0^+)$, were converted to $R_0(\lambda)$ prior to calibration according to (Pitarch et al., 2019; Zeng et al., 2017):

$$R_0(\lambda) = Q \cdot R_{RS}(\lambda, 0^+) / \left(0.52 + 1.7 \cdot R_{RS}(\lambda, 0^+)\right), \quad (13)$$

This allows the calibration algorithm to compare the observations directly with the corresponding optical variable calculated by the model at each simulation ($R_0(\lambda)$), while the conversion of the modelled $R_0(\lambda)$ to $R_{RS}(\lambda)$ (Eq. 12) is retained for post-processing and comparison with the original satellite product.

The Differential Evolution algorithm was configured with a differential weight (F) of 0.5 and a crossover probability (Cr) of 0.9, following the configuration used by Álvarez et al. (2023). The stopping criterion for the GA was a maximum number of 90 generations in the main GA experiment and 40 and 60 generations in the GA targeted experiments at BOUSSOLE and AAOT, respectively.

2.4.2 Validation

Model validation was performed using observational datasets that were independent of those used for calibration. Whereas $R_{RS}(\lambda)$ from the MULTI-sensor dataset was used in the GA, validation was carried out using $R_{RS}(\lambda)$ outside of the calibration period, as well as $R_{RS}(\lambda)$ from the OLCI-sensor, OC-derived Chl and $b_{bp}(443)$. To ensure comparability with the ocean-colour-derived products, simulated variables other than $R_{RS}(\lambda)$ were vertically averaged over the first optical depth (FOD). The FOD was defined as $z_{EU}/4.6$, where z_{EU} is the euphotic depth, corresponding to the depth at which photosynthetically active radiation (PAR) decreases to 1% of its value in the first model layer. Additional validation data included in situ Chl, phytoplankton C and $b_{bp}(\lambda)$. In situ observations were vertically averaged over the upper 12 m at BOUSSOLE and the upper 6.5 m at AAOT.

https://doi.org/10.5194/egusphere-2026-6687
Preprint. Discussion started: 5 November 2026
© Author(s) 2026. CC BY 4.0 License.

3 Results

3.1 Sensitivity analysis (SA)

The aim of the sensitivity analysis was to identify which model parameters most strongly control the simulated optical behaviour of surface waters. **Figure 2** and **Figure 3** show the ranks of parameters influencing $R_0(\lambda)$, and concentrations of phytoplankton Chl and C at surface in the well-mixed season (winter, upper panels) and in the stratified season (summer, lower panels), among the total of 248 tested for the BOUSSOLE site and the total of 254 tested for the AAOT site. The horizontal bars show, for each parameter included in the analysis, the absolute value of the sensitivity coefficient βi that indicates whether an increment or decrement in the value of the parameter has an effect on the targeted output. Only parameters with $|\beta i|$ larger than the 30% of the maximum $|\beta i|$ for each targeted output are displayed. The color of the bar codes the model component the parameter relates to, among phytoplankton, detritus, CDOM, bacteria, zooplankton and SPM. The overall fraction of the model output variability (R^2) that is explained by the multiple linear regression is shown on top of the rank for each targeted output.

At BOUSSOLE, the shorter wavebands of the $R_0(\lambda)$ spectrum were influenced mostly by CDOM parameters, both in winter and summer (yellow bars, **Fig. 2**), whereas for bands longer than 450 nm phytoplankton parameters are the most influential (green bars, **Fig. 2**). On the other hand, concentrations of Chl and C at surface were influenced by phytoplankton and microzooplankton parameters in winter (green and grey bars, **Fig. 2a**) and almost exclusively by bacteria parameters in summer (red bars, **Fig. 2b**).

At AAOT, both short and long wavebands of the $R_0(\lambda)$ spectrum were influenced exclusively by SPM in winter (blue bars, **Fig. 3a**) and mostly by SPM with some influence of microzooplankton ($Z^{(5)}$) on the bands longer than 600 nm in summer (blue and grey bars, **Fig. 3b**). Similarly to BOUSSOLE, the parameters influencing the concentrations of Chl and phytoplankton C at surface in winter were those related to phytoplankton ($P^{(2)}$ and $P^{(3)}$, green bars, **Fig. 3a**) and microzooplankton ($Z^{(5)}$, grey bars, **Fig. 3a**) and in summer were predominantly bacteria (red bars, **Fig. 3b**) with some influence of $P^{(3)}$ and $Z^{(5)}$ in the case of [Chl] and $Z^{(5)}$ and $Z^{(6)}$ in the case of [C].

https://doi.org/10.5194/egusphere-2026-6687
Preprint. Discussion started: 5 November 2026
© Author(s) 2026. CC BY 4.0 License.

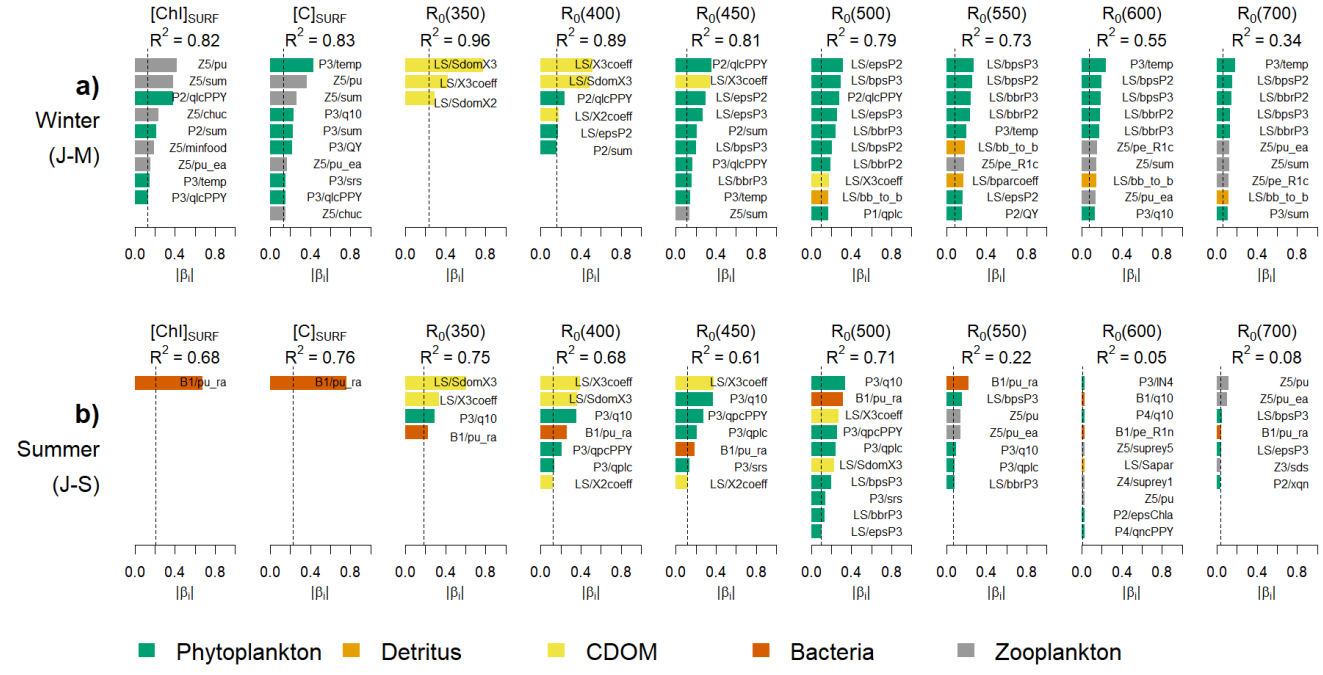


Figure 2: Sensitivity ranks BOUSSOLE: sensitivity of [Chl], phytoplankton [C] and $R_0(\lambda)$ output (|βi| in x-axis) to perturbation of parameters (y-axis) during a) winter (January to March) and b) summer (July to September) periods. $P^{(1)}$ to $P^{(4)}$ state for instances of primary producers, $Z^{(3)}$ to $Z^{(6)}$ for instances of consumers, $B^{(1)}$ for the only instance of bacteria and LS for the module light_spectral. For each output, R^2 indicates the overall fraction of the model output variability that is explained by the perturbation of parameter values. Only parameters with |βi| larger than the 30% of the first-ranked parameter |βi| within each targeted output (vertical dashed line) are shown. The nomenclature for the complete list of parameters can be consulted in Table A1 in Appendix A.

https://doi.org/10.5194/egusphere-2026-6687
Preprint. Discussion started: 5 November 2026
© Author(s) 2026. CC BY 4.0 License.

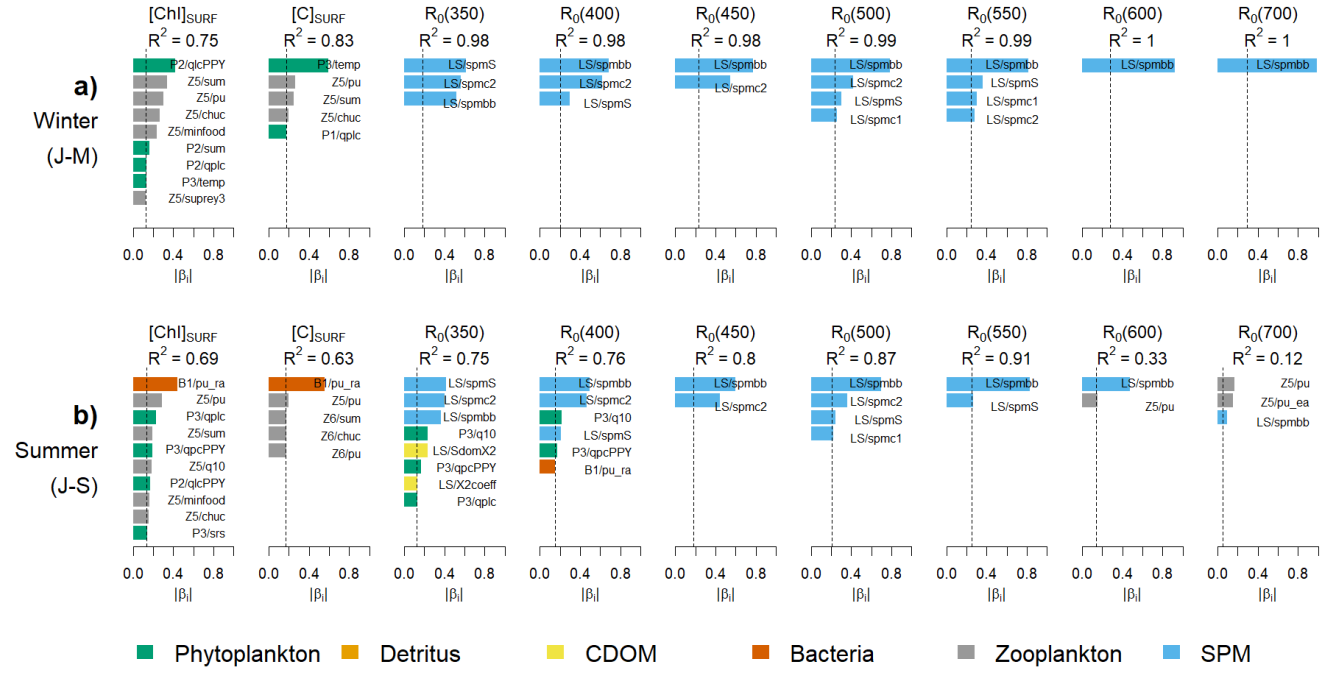


Figure 3: Sensitivity ranks AAOT: sensitivity of [Chl], phytoplankton [C] and $R_0(\lambda)$ output ($|\beta i|$ in x-axis) to perturbation of parameters (y-axis) during a) winter (January to March) and b) summer (July to September) periods of 2012. The names of the model instances are the same as in Figure 2. Unlike BOUSSOLE, the categories of parameters include SPM.

3.2 Calibration of parameters (GA)

The 12 most influential parameters at BOUSSOLE were: four related to picophytoplankton, two that control their regulation by temperature ($P^{(3)}$/q10, $P^{(3)}$/temp) and two that set their scattering behaviour (bpsP3 and bbrP3); one for bacteria that sets their activity respiration fraction ($B^{(1)}$/pu_ra); three for microzooplankton, their maximal growth rate ($Z^{(5)}$/sum) and two related to their efficiency assimilating food ($Z^{(5)}$/pu, $Z^{(5)}$/pu_ea); two for CDOM, both controlling the optical behaviour of the refractory pool (SdomX3 and X3coeff) and two related to nanophytoplankton, their reference Chl to C quotum ($P^{(2)}$/qlcPPY) and their mean absorption cross section (epsP2). **Table 2** shows the range of parameter values given at the start of the calibration and the value that converged after 90 generations.

At AAOT, the 12 most influential parameters were: four controlling the optical behaviour of SPM (spmbb, spmc2, spmS and spmc1); four for picophytoplankton, the two that control their regulation by temperature ($P^{(3)}$/q10, $P^{(3)}$/temp) and their minimum and reference P to C quota ($P^{(3)}$/qplc, $P^{(3)}$/qpcPPY); one for bacteria that sets their activity respiration fraction ($B^{(1)}$/pu_ra); two for microzooplankton related to their efficiency assimilating food ($Z^{(5)}$/pu and $Z^{(5)}$/pu_ea); and one for

https://doi.org/10.5194/egusphere-2026-6687
Preprint. Discussion started: 5 November 2026
© Author(s) 2026. CC BY 4.0 License.

nanophytoplankton, their reference Chl to C quotum ($P^{(2)}$/qlcPPY). **Table 3** shows the range of parameter values given at the start of the calibration and the value that converged after 90 generations.

Table 2: Rank of parameters at the BOUSSOLE site, units, ranges given for optimization and optimized value obtained.

Instance/parameter	Description	Units	Min. value	Max. value	Optim. value
$P^{(3)}$/q10	temperature Q10 coefficient	-	1.0	2.0	1.02527
$P^{(3)}$/temp	cut-off threshold for temperature factor	-	0.50	1.0	0.662684
$P^{(2)}$/qlcPPY	reference quotum Chl:C	mg Chl mg C^{-1}	0.01	0.06	0.0496934
$B^{(1)}$/pu_ra	activity respiration fraction	-	0.75	1.0	0.955604
$Z^{(5)}$/sum	potential specific growth rate at 10ºC	d^{-1}	2.0	5.5	5.16168
$Z^{(5)}$/pu	assimilation efficiency	-	0.35	0.65	0.505131
$Z^{(5)}$/pu_ea	excreted fraction of uptake	-	0.35	0.75	0.467002
LS/SdomX3	CDOM absorption spectral slope	nm^{-1}	0.015	0.021	0.0196122
LS/X3coeff	mass-specific absorption coefficients of CDOM	m^2 mg C^{-1}	0.004	0.018	0.00545734
LS/epsP2	Chl-specific mean absorption cross-section of $P^{(2)}$	m^2 mg Chl^{-1}	0.010	0.050	0.0439613
LS/bpsP3	C-specific mean scattering cross-section of $P^{(3)}$	m^2 mg C^{-1}	0.006	0.060	0.0187035
LS/bbrP3	$P^{(3)}$ backscatter to total scatter ratio	-	0.003	0.030	0.0032797

Table 3: Rank of parameters at the AAOT site, units, ranges given for optimization and optimized value obtained.

Instance/parameter	Description	Units	Min. value	Max. value	Optim. value
LS /spmbb	SPM mass-specific backscattering at 555nm	m^2 g^{-1}	0.003	0.02	0.00477547
LS /spmc2	SPM mass-specific absorption at 440nm	m^2 g^{-1}	0.024	0.05	0.0240401
LS /spmS	slope for exponential decline of SPM absorption with wavelength	nm^{-1}	0.011	0.013	0.012862
LS /spmc1	basal absorption for minimal absorption at long wavelengths	m^2 g^{-1}	0.001	0.010	0.00102525
$P^{(3)}$/q10	temperature Q10 coefficient	-	1.0	2.0	1.99843
$P^{(3)}$/temp	cut-off threshold for temperature factor	-	0.5	1.0	0.838237
$P^{(3)}$/qplc	minimum quotum P:C	mmol P mg C^{-1}	0.00024	0.00050	0.000497
$P^{(3)}$/qpcPPY	reference quotum P:C	mmol P mg C^{-1}	0.00055	0.00110	0.000655
$B^{(1)}$/pu_ra	activity respiration fraction	-	0.75	1.0	0.99983
$Z^{(5)}$/pu	assimilation efficiency	-	0.35	0.65	0.355379
$Z^{(5)}$/pu_ea	excreted fraction of uptake	-	0.35	0.75	0.35641
$P^{(2)}$/qlcPPY	reference quotum Chl:C	mg Chl mg C^{-1}	0.01	0.06	0.0137198

https://doi.org/10.5194/egusphere-2026-6687
Preprint. Discussion started: 5 November 2026
© Author(s) 2026. CC BY 4.0 License.

The trajectories of the RMSE for the six $R_0(\lambda)$ observations included in the cost function are shown for BOUSSOLE (**Fig. 4a**) and AAOT (**Fig. 4b**) as a function of the 90 generations run. For BOUSSOLE, after approximately 70 generations the RMSE of all wavebands decreased below 0.01 (unitless), with larger errors occurring at shorter wavelengths, which consistently exhibit higher values across the $R_0(\lambda)$ spectrum at an open ocean site such as BOUSSOLE. For AAOT, after approximately 40 generations, the RMSE remained between 0.01 and 0.025, showing the larger errors at intermediate wavelengths (490 and 510 nm) which are the ones that more frequently have the larger values of the spectrum in a land-influenced site as AAOT. The optimization trajectories of the 12-sets of parameter values of BOUSSOLE and AAOT are available in Appendix B **Figs. B1** and **B2**, respectively.

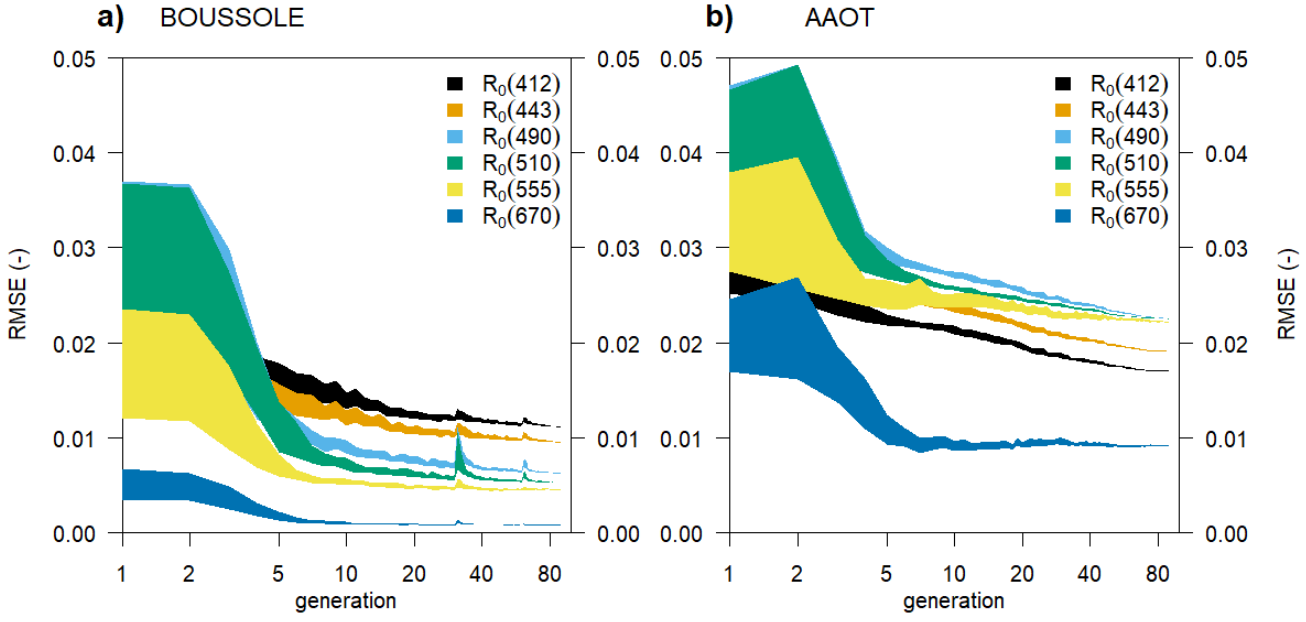


Figure 4: Calibration trajectories of the root mean square error (RMSE) of $R_0(\lambda)$ wavebands (model vs. MULTI-sensor CMS) as a function of the number of generations run in the GA optimization for a) BOUSSOLE and b) AAOT.

https://doi.org/10.5194/egusphere-2026-6687
Preprint. Discussion started: 5 November 2026
© Author(s) 2026. CC BY 4.0 License.

3.3 Spectra of simulated $R_{RS}(\lambda)$ vs. non-GA-used $R_{RS}(\lambda)$

After optimization, we explored how the $R_0(\lambda)$-calibrated model was able to reproduce $R_{RS}(\lambda)$ from the same sensor (MULTI-sensor) with independent data of a posterior period of time (4 years after GA) and from a different sensor (OLCI-sensor). **Figure 5** shows the $R_{RS}(\lambda)$ spectra model simulated (in color) and retrieved by the MULTI-sensor (black) and the OLCI-sensor (grey) CMS products, both in winter (left panels) and summer (right panels) at the BOUSSOLE (top panels) and the AAOT (bottom panels) sites. The same results disaggregated by month can be consulted in Appendix B **Fig. B3**.

For BOUSSOLE, the simulated $R_{RS}(\lambda)$ spectra aligns with the MULTI-sensor product both in winter (**Fig. 5a**) and in summer (**Fig. 5b**) whereas the OLCI-sensor product tends to give slightly larger values in the wavebands between 400 and 450 nm. Therefore, the model is able to reproduce the characteristic spectra of blue waters peaked at 400 nm and that are flatter in winter than in summer.

For AAOT, the MULTI-sensor and OLCI-sensor products are relatively well aligned both in winter and summer. In winter, the simulated $R_{RS}(\lambda)$ spectrum tends to underestimate the satellite products between 400 and 600 nm, aligns relatively well between 625 and 675 nm, and underestimated the OLCI-sensor product on bands longer than 700 nm (**Fig. 5c**). In summer, the model $R_{RS}(\lambda)$ aligns relatively well in the shorter band (400 nm) and for bands longer than 625 nm, but tends to overestimate $R_{RS}(\lambda)$ between 425 and 600 nm (**Fig. 5d**). Overall, the model is able to reproduce the characteristic spectra of turbid waters peaked around 500 nm and that are flatter in summer than in winter.

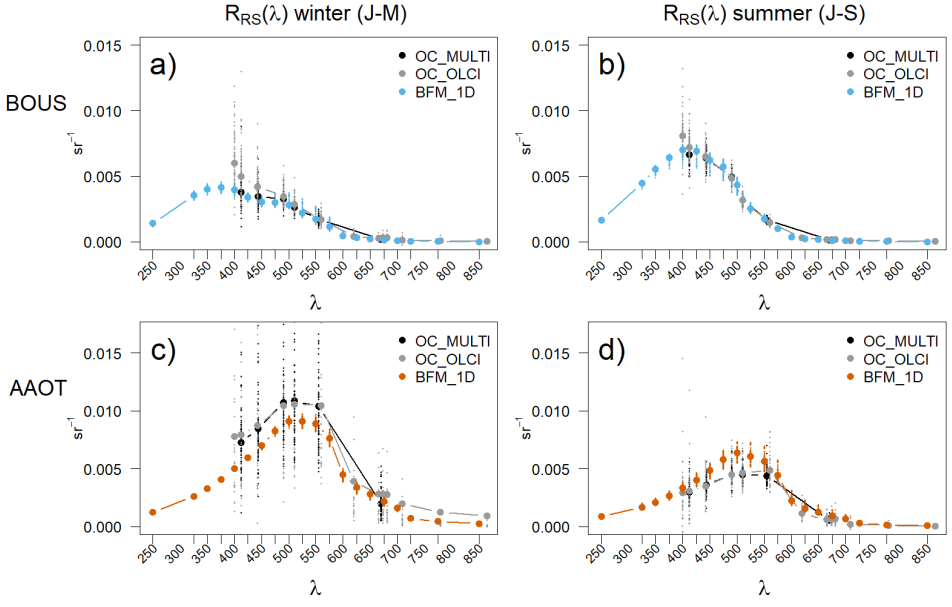


Figure 5: Four-years average of $R_{RS}(\lambda)$ at BOUSSOLE (2017-2020) and AAOT (2014-2017) in a) winter and b) summer from CMS MULTI-sensor (black) and OLCI-sensor (grey) products, and from the optimized model output. The same results disaggregated by month in Appendix B Fig. B3. Note that the OLCI product in AAOT only covers 2017.

https://doi.org/10.5194/egusphere-2026-6687
Preprint. Discussion started: 5 November 2026
© Author(s) 2026. CC BY 4.0 License.

3.4 Non-GA-used biogeochemical & optical variables

The timeseries of non-GA-used $R_{RS}(\lambda)$ at BOUSSOLE (**Fig. 6**, left panels) and AAOT (**Fig. 7**, left panels) show that, after GA calibration, the modelled $R_{RS}(\lambda)$ approximates to the MULTI-sensor observed $R_{RS}(\lambda)$. However, the fit is not perfect, the model fails to capture the winter to summer transition in the shorter wavelengths (<510nm) and generally underestimates $R_{RS}(\lambda)$ in the second half of the year for longer wavebands (**Fig. 6**). At AAOT, the larger discrepancies occur in the shorter wavelengths, where the model does not reach the winter maxima nor the summer minima (**Fig. 7**). The complete set of $R_{RS}(\lambda)$ wavebands at BOUSSOLE and AAOT are available in Appendix B **Figs. B4** and **B5**, respectively.

We explored how the $R_0(\lambda)$-calibrated model was able to reproduce other non-used in GA optical and biogeochemical variables, by comparing model output with ocean colour (OC-) based and in situ estimates of those variables at BOUSSOLE (**Fig. 6**, right panels) and AAOT (**Fig. 7**, right panels). The timeseries (NPP) and profiles of other relevant biogeochemical variables (phytoplankton carbon, Chl, DIN, and DIP) simulated before and after the GA optimization at BOUSSOLE and AAOT are available in Appendix B **Figs. B6** and **B7**, respectively.

At BOUSSOLE, the calibration with $R_0(\lambda)$ moved Chl to larger concentrations in surface during summer (**Fig. 6d**). The tendency of BFM-based Mediterranean configurations to underestimate surface Chl during summer has also been reported for the operational MedBFM system (Feudale et al., 2022). However, the MedBFM system assimilates satellite Chl, so its performance is not necessarily representative of an unconstrained BFM simulation, as the one used in this work. The calibration also moved phytoplankton [C] up (**Fig. 6e**) which is basically the reason the model is able to reproduce the summer maxima of $R_{RS}(\lambda)$ in the shorter wavebands (**Fig. 6a-b**). For the longer wavebands of the $R_{RS}(\lambda)$ spectrum, the model approximates observations (**Fig. 6c**) as $b_{bp}(443)$ increases given the increase in phytoplankton [C] (**Fig. 6f**). However, $b_{bp}(443)$ is still largely underestimated out of the spring bloom.

https://doi.org/10.5194/egusphere-2026-6687
Preprint. Discussion started: 5 November 2026
© Author(s) 2026. CC BY 4.0 License.

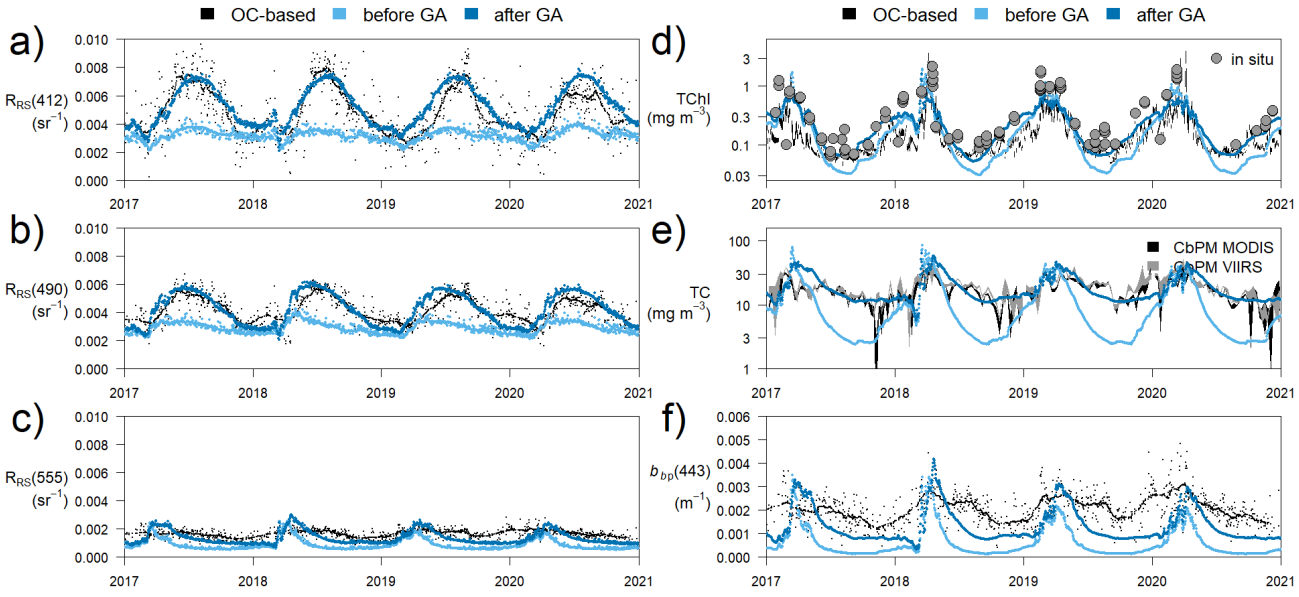


Figure 6: GA-used vs. non-GA-used variables at BOUSSOLE in the first optical depth (FOD): 2017-2020 timeseries of a) $R_{RS}(412)$, b) $R_{RS}(490)$ and c) $R_{RS}(555)$ simulated before (light blue) and after (dark blue) GA with the 2013-2016 timeseries; 2017-2020 timeseries of the non-GA-used: d) Chl, e) phytoplankton C and f) $b_{bp}(443)$. Each modelled variable is compared to their OC-based counterpart, all obtained from CMS products (black) except the CbPM output in panel e) (from MODIS in grey, from VIIRS in black). In d), the dots show the field measured total Chl averaged in the first 12 m of the water column (average of the FOD, computed as zeu/4.6).

At AAOT, calibration with $R_0(\lambda)$ increased the simulated surface Chl concentrations to slightly larger values during summer, but Chl remained substantially underestimated relative to the satellite-derived observations (**Fig. 7d**). Although part of this discrepancy could reflect differences between satellite and in situ Chl, including the spatial representativeness of the satellite product, the concurrent underestimation of phytoplankton carbon (**Fig. 7e**) provides independent evidence of a deficit in simulated phytoplankton biomass. Unlike BOUSSOLE, simulated $b_{bp}(443)$ aligns pretty well with the OC-based counterpart (**Fig. 6f**), even when phytoplankton [C] is not well captured, in agreement with the fact that the main source of particle backscattering at the site is the non-algal suspended material. Note there is one order of magnitude difference in $b_{bp}(443)$ with respect to BOUSSOLE.

https://doi.org/10.5194/egusphere-2026-6687
Preprint. Discussion started: 5 November 2026
© Author(s) 2026. CC BY 4.0 License.

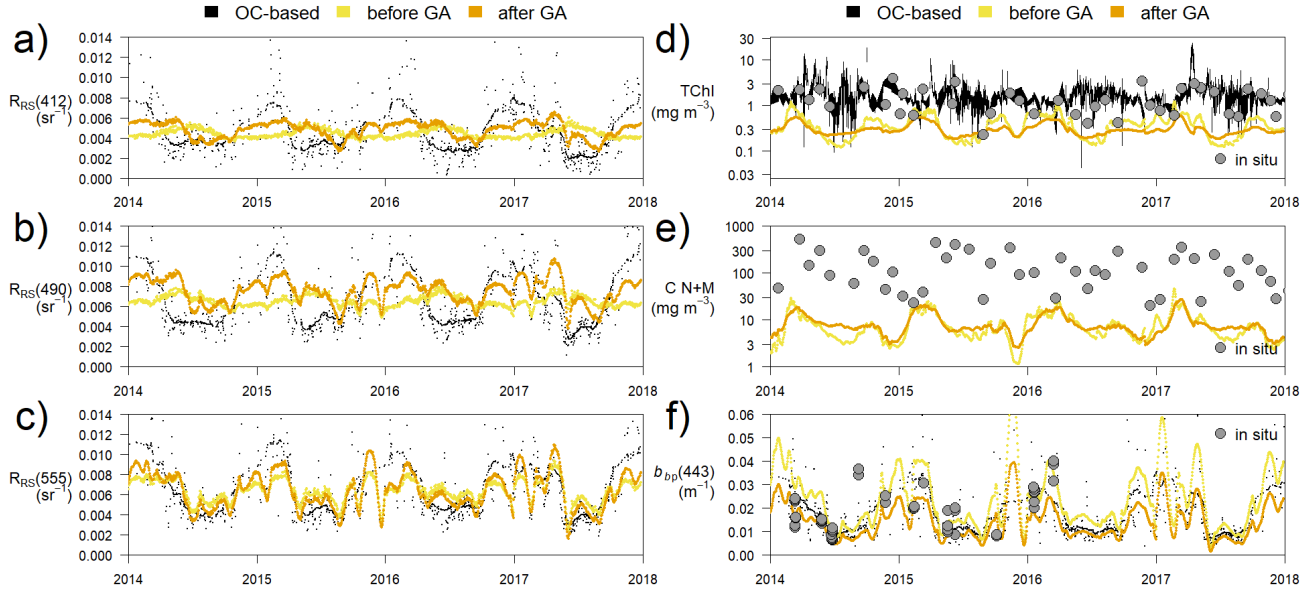


Figure 7: GA-used vs. non-GA-used variables at AAOT: 2014-2017 timeseries of a) R_{RS}(412), b) R_{RS}(490) and c) R_{RS}(555) simulated before (light blue) and after (dark blue) calibration of the 2010-2013 timeseries. Each modelled variable is compared to their OC-based counterpart, all obtained from CMS products (black). Simulated average in the first 6.5m of the non-GA-used d) Chl, e) phyto>2µm C and f) b_{bp}(443). The black lines in d) and f) indicate OC-based counterparts, all obtained from CMS products. The dots in d) and e) show field-measured TChl-a and carbon of nano- and micro-phytoplankton, respectively (collection depth <6.5m). The dots in f) indicate b_{bp}(442) measurements provided by the near-surface CoASTS-BiOMaP dataset (1m depth).

3.5 Sensitivity to optical model assumptions

The independent validation (Sect. 3.3 and 3.4) shows that the GA optimization procedure substantially improves model performance compared to the baseline configuration. However, some systematic mismatches between the simulated optical and biogeochemical properties persisted. In particular, at BOUSSOLE, the calibrated model substantially improved the representation of phytoplankton carbon, whereas particulate backscattering b_{bp}(443 nm) remained underestimated, mostly in summer. At AAOT, in contrast, the optical signal was largely dominated by SPM, potentially masking the contribution of phytoplankton to the simulated $R_{RS}(\lambda)$. These contrasting results suggested that some of the remaining discrepancies could not be fully resolved through the calibration of the selected parameters alone, but could instead reflect simplifications in the representation of the interactions between biogeochemical constituents and light.

To address these limitations, we therefore performed a set of targeted numerical experiments to investigate the influence of two model assumptions on the simulated optical properties. At BOUSSOLE, we examined the consequences of neglecting

https://doi.org/10.5194/egusphere-2026-6687
Preprint. Discussion started: 5 November 2026
© Author(s) 2026. CC BY 4.0 License.

the interaction of heterotrophic bacteria with light, given their potential contribution to the pool of small non-algal particles and, consequently, to particulate scattering and backscattering. At AAOT, we investigated the assumption of spectrally independent SPM scattering and backscattering. To isolate the effects of these assumptions, we manually perturbed the magnitude and spectral dependence of the scattering properties of bacteria ($B^{(1)}$) at BOUSSOLE and of SPM at AAOT, while holding the rest of the optical parameters at calibrated values.

3.5.1 BOUSSOLE: Including bacteria scattering (bB1, bbB1 and their spectral slopes)

A recent analysis of biogeochemical property retrievals in seawater, based on the inversion of the three-stream irradiance model at the BOUSSOLE site, highlighted the difficulty of reconciling model-derived and observed $b_{bp}(\lambda)$ values, particularly for $b_{bp}(443)$ during the summer period (Lazzari et al., 2024). Here, we propose a solution to this inconsistency by extending the set of optical constituents beyond the standard ones (phytoplankton, CDOM, and NAP) in a GA fine-tuning experiment at the BOUSSOLE site. We explored whether small non-algal particles such as bacteria may represent an important source of $b_{bp}(\lambda)$ at the site, and whether including their impact on light can improve the representation of $b_{bp}(443)$. To do that, and starting from parameter ranges reported in the literature (Serra-Pompei et al., 2023; Stramski et al., 2001; Vaillancourt et al., 2004), the scattering and backscattering coefficients of bacterial carbon (bB1 and bbB1, m^2 mg C^{-1}) at 555 nm, as well as their spectral slopes (bSB1 and bbSB1, nm^{-1}) were allowed to vary. The ranges of parameter values explored and their optimization trajectories are shown in Appendix B **Fig. B8**. Bacterial absorption was neglected.

The parameters converged toward values that remain within plausible ranges for small non-algal particles, both in magnitude and in spectral dependencies (**Fig. 8a-b**), although in natural conditions they have reported a large variability. This fine-tuning led to an improved representation of $b_{bp}(443)$ (**Fig. 8d**), particularly during periods when the model previously underestimated $b_{bp}(\lambda)$ (i.e. summer). Although these results are merely exploratory, they suggest that the current bio-optical parameterization may underestimate the contribution of small particles to total $b_{bp}(\lambda)$ in oligotrophic open-ocean conditions. Given the low magnitude of $b_{bp}(443)$ at the site, R_{RS} at 443 was only minorly impacted (**Fig. 8c**). An additional simulation where bacteria scattering was not considered but the b_b to b ratio of picophytoplankton (bbrP3) was increased to 0.005 (pink in **Fig. 8b**), shows that although increasing effective backscattering from small phytoplankton increases $b_{bp}(443)$, it does not change its seasonality and therefore does not correct the difference between the spring maxima and the summer minima (pink line in **Fig. 8d**).

https://doi.org/10.5194/egusphere-2026-6687
Preprint. Discussion started: 5 November 2026
© Author(s) 2026. CC BY 4.0 License.

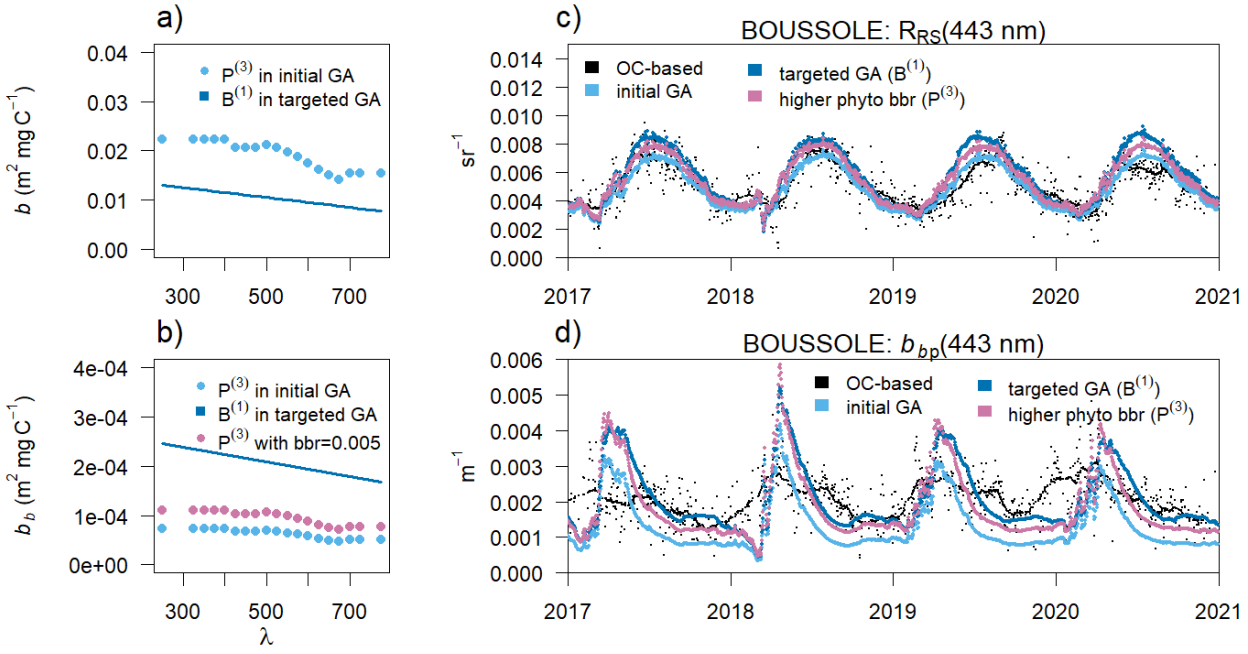


Figure 8: GA fine-tuning experiment at BOUSSOLE including the interaction of bacteria with light: spectral dependencies of a) scattering and b) backscattering coefficients for $B^{(1)}_C$ and $P^{(3)}_C$. Note that the $b(\lambda)$ and $b_b(\lambda)$ spectra of picophytoplankton ($P^{(3)}$) have the same spectral dependency because the b_b:b ratio is spectrally independent for the phytoplankton groups. Model output at 443 nm of c) R_{RS} and d) b_{bp} in the initial GA optimization (light blue), the GA optimized simulation with scattering from $B^{(1)}$ (dark blue) and the ad-hoc simulation with a higher b_b to b ratio for $P^{(3)}$ (pink).

3.5.2 AAOT: Fine-tuning of SPM scattering (b, b_b and their spectral slopes)

The sensitivity analysis identified the optical parameters of SPM as the dominant controls on $R_{RS}(\lambda)$ at AAOT (Sect. 3.1). Accordingly, the GA calibration substantially modified these parameters (Sect. 3.2) and improved the agreement with the observed $R_{RS}(\lambda)$ (Section 3.3), but these improvements were not accompanied by a comparable improvement in the simulated Chl concentration or phytoplankton carbon (Sect. 3.4). This result raised the possibility that the high sensitivity of $R_{RS}(\lambda)$ to SPM optical properties allowed the calibration to compensate for discrepancies in other optically active components, particularly phytoplankton. To explore this possibility, we performed a targeted GA fine-tuning experiment in which the magnitude of the SPM scattering and backscattering coefficients at 555 nm (spmb and spmbb, respectively, **Table A1**) were allowed to vary, together with their spectral dependencies around 555 nm (bSSPM and bbSSPM, nm^{-1}). This provided additional degrees of freedom to the SPM optical representation and allowed us to test whether further improvement in the fit to the six-wavelength $R_{RS}(\lambda)$ could be achieved through SPM properties alone. The ranges of parameter values explored and their optimization trajectories are shown in Appendix B **Fig. B9**.

https://doi.org/10.5194/egusphere-2026-6687
Preprint. Discussion started: 5 November 2026
© Author(s) 2026. CC BY 4.0 License.

The optimized b_b to b ratio at 555 nm (~0.025) (**Fig. 9a–b**) is close to b_b to b ratios typically reported for coastal waters rich in mineral particles. Moreover, the optimized spectral slope of $b_b(\lambda)$ is only slightly negative (**Fig. 9b**), indicating a weak decrease toward the red, which is broadly consistent with observations of natural particle assemblages (Stramski et al., 2001). On the other hand, the GA produced a positive and unrealistically steep spectral slope for b, which increases scattering toward the red and strongly decreases it toward the blue (**Fig. 9b**). This adjustment improved the model representation of $b_{bp}(443)$ (**Fig. 9d**), but such a spectral behaviour is not expected for natural particle populations. Instead, it likely acts as a compensating mechanism within the GA optimization, that arises because spmb and spmbb of SPM are optimized independently, allowing the b_b:b ratio to vary freely and reaching values that may not be physically realistic. The resulting increase in b_b:b suggests that the model requires a higher effective backscattering efficiency in order to reproduce the observed $R_{RS}(\lambda)$. This indicates that the current parameterization of SPM does not provide sufficient flexibility to represent the optical variability of the system, and highlights potential structural limitations of the bio-optical model, particularly regarding the representation of algal and non-algal particle backscattering and particle size distribution in turbid waters.

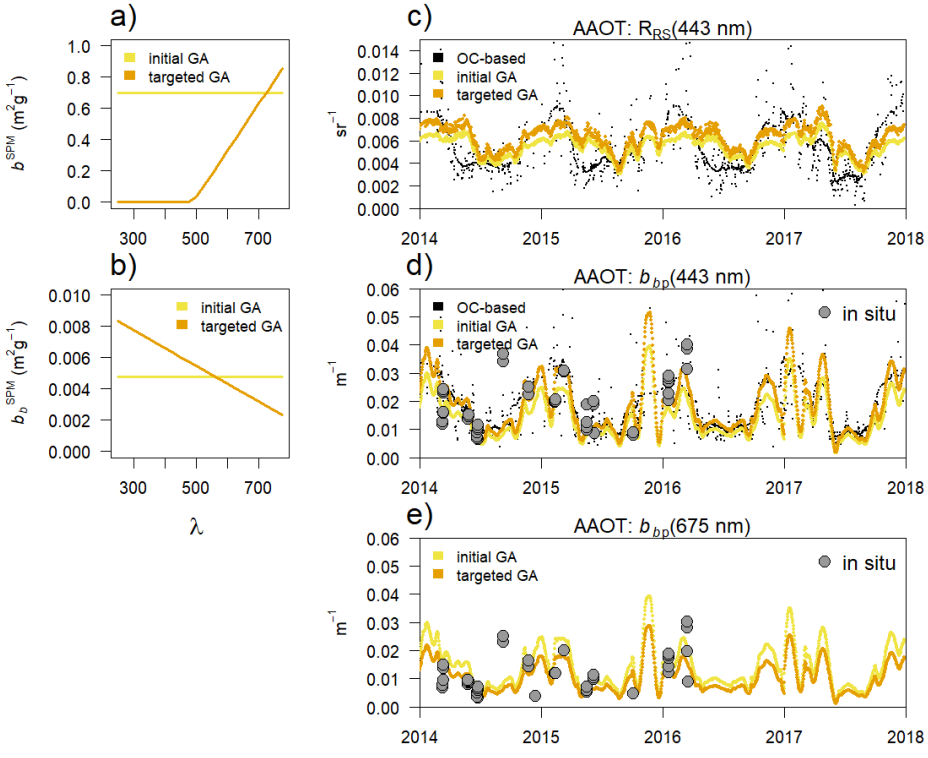


Figure 9: GA fine-tuning experiment at AAOT perturbing the spectral dependencies of SPM a) scattering and b) backscattering coefficients. Model output for c) R_{RS}(443 nm), d) b_{bp}(443 nm) and d) b_{bp}(675 nm) in the initial GA optimization (yellow) and after the targeted GA optimization (orange) of SPM parameters. Panels d) and e) show their CMS OC-based counterparts (black), and the dots in panels d) and e) show b_{bp} measurements at 442 and 676 nm, respectively, provided by the near-surface CoASTS-BiOMaP dataset (1m depth).

https://doi.org/10.5194/egusphere-2026-6687
Preprint. Discussion started: 5 November 2026
© Author(s) 2026. CC BY 4.0 License.

4 Discussion and conclusions

Remote-sensing reflectance of the ocean ($R_{RS}(\lambda)$), the main quantity retrieved by ocean-color sensors after atmospheric correction, is a highly aggregated signal. It represents the combined influence of many in-water constituents on the way light is scattered and absorbed before leaving the water surface. The strength of this aggregated nature is that the $R_{RS}(\lambda)$ spectrum encodes rich information about the composition and state of the marine environment, making it possible to infer ecological and/or biogeochemical properties from space. The drawback, however, is that because these influences are tightly entangled, deconvolving the contributions of individual constituents is challenging, often requiring sophisticated models, assumptions, or ancillary data to resolve the underlying complexity.

As new ocean color sensors with improved capabilities for hyperspectral optical remote sensing become operational (e.g. PRISMA, EnMAP, PACE), they provide potentially powerful means for monitoring open ocean and coastal waters at various space and time scales. They have the potential to be used directly on OC-based applications (IOCCG, 2026) and/or be incorporated into process-based BGC models, transferring ocean-colour information to the biogeochemical domain (Ciavatta et al., 2014). Several case studies report improved match to both remote and in situ optical variables when $R_{RS}(\lambda)$ (or IOPs derived by inversion) are used as the assimilated observable (Jones et al., 2016; Lazzari et al., 2024).

Following this community effort, in this work we show how integrating the processes-based BFM with OC-observations ($R_{RS}(\lambda)$) through formal calibration procedures is useful to improve the agreement with observed $R_{RS}(\lambda)$ and how these improvements translate to other optical and biogeochemical variables. The process-based BFM is able to ingest such information thanks to (1) its extension with optical components, and (2) the formal techniques matched to the framework for model calibration (Bruggeman and Bolding, 2020), data assimilation (Bruggeman et al., 2024) and inversion (Lazzari et al., 2024).

At the oceanic BOUSSOLE site, the modifications in parameter values that take $R_{RS}(\lambda)$ more successfully to their summer maxima (**Fig. 6a-b**) are those increasing the concentrations of phytoplankton carbon in superficial layers in summer (**Fig. 6e**). These phytoplankton carbon concentrations match those provided by the OC-based CbPM (Westberry et al., 2008) for the site. This supports the idea that, in the open ocean, the R_{RS}-based improvements translated pretty directly to the biogeochemical domain. In absence of field-based measurements, however, it is uncertain if the corrected backscattering is indeed caused by more phytoplankton biomass, or could be correcting an incomplete connection between other water components and IOPs. The increase in carbon concentrations contribute to move $b_{bp}(443)$ closer to the OC-based estimates, but $b_{bp}(443)$ is still largely underestimated in summer (**Fig. 6f**). Bacteria and other submicron particles could be an important source of backscattering (Martinez-Vicente et al., 2012; Serra-Pompei et al., 2023), relevant specially during the warmer months. Bio-optical models tend to underestimate $b_{bp}(\lambda)$ in oligotrophic waters because they do not represent well submicron particles (bacteria, submicron detritus…). GOTM-BFM, in particular, does not consider the light scattered by bacteria or in general any living particle smaller than cyanobacteria. When the light scattered by bacteria is considered, the underestimation is partially corrected (**Fig. 8d**).

https://doi.org/10.5194/egusphere-2026-6687
Preprint. Discussion started: 5 November 2026
© Author(s) 2026. CC BY 4.0 License.

In addition to the potential contribution of bacteria to the underestimated particulate backscattering, other sources may be associated with larger particles that are not explicitly or fully represented in the model and that could be targeted for future model developments. In particular, the optical contribution of phytoplankton may depend not only on their concentration but also on their particle-level structural characteristics, including cell size, shape, internal structure and refractive index (Organelli et al., 2018). This complexity may influence their scattering and backscattering properties and is only partially captured by the simplified representation of phytoplankton optical properties adopted here. Zooplankton may also contribute to the particulate backscattering signal, either directly as scattering particles or indirectly through their production of detrital material and other large particles (Davies et al., 2021).

At the AAOT coastal site, where mineral/detrital SPM dominates the scattering signal, the broad improvement in $R_{RS}(\lambda)$ (**Fig. 6a-b**) was achieved through substantial adjustments to SPM optical parameters (Appendix B **Fig. B2**). The residual sensitivity of $R_{RS}(\lambda)$ to the phytoplankton parameters is small compared with the SPM signal and the observational noise, making the phytoplankton optical signal a small and potentially confounded component of the total $R_{RS}(\lambda)$. Consequently, phytoplankton Chl and C were only slightly moved during calibration (**Fig. 6d-e**).

This result suggests that an improvement in $R_{RS}(\lambda)$ does not necessarily translate into an equivalent improvement in the representation of the underlying biogeochemical state, particularly when there is strong overlap between the optical contributions of different particle pools. Moreover, our targeted fine-tuning experiments showed that the fit to $R_{RS}(\lambda)$ could be further improved through additional adjustments to SPM optical properties (**Fig. 9**). This indicates that the SPM parameters retained sufficient flexibility to account for additional spectral variability, raising the possibility that they may compensate for unresolved contributions from other biogeochemical components. Such compensation could improve the optical fit while producing parameter values that are difficult to interpret physically and without necessarily improving the representation of phytoplankton biomass. Where suspended particulate matter dominates the scattering signal, spectrum-level calibration of $R_{RS}(\lambda)$ must probably be complemented by additional phytoplankton-sensitive observables (e.g., fluorescence, in-water $b_{bp}(\lambda)$ profiles). Incorporating such complementary observations could help constrain the contributions of different particle pools, reduce parameter compensation, and improve the reliability of the inferred biological state.

It is worth mentioning, however, that the current model configuration prescribes SPM as a vertically uniform concentration derived from satellite observations, rather than representing it as a dynamically evolving component of the water column. This is a relevant simplification for shallow coastal systems, where processes such as sediment resuspension, particle settling, aggregation, and disaggregation can strongly modify both the vertical distribution and size structure of suspended particles (Fettweis et al., 2026), and consequently their scattering and backscattering properties. The GA calibration experiments suggest that the model may partly compensate for this structural limitation through adjustments of the SPM optical parameters, including elevated backscattering ratios that may be physically difficult to reconcile. This result points to the potential benefit of explicitly representing SPM dynamics, including its vertical transport and particle-size distribution. A

https://doi.org/10.5194/egusphere-2026-6687
Preprint. Discussion started: 5 November 2026
© Author(s) 2026. CC BY 4.0 License.

more explicit representation of SPM dynamics and particle-size-dependent optical properties could therefore provide additional constraints on the optical signal and reduce the need for compensatory adjustments of SPM parameters.

Although there is in BFM, and other bio-optical models, already a remarkable fidelity in the model connections to fields such as $R_{RS}(\lambda)$, challenges persist when trying to compare model output, satellite products and field-based data (IOCCG, 2020). In this study, satellite products were spatially averaged over a 20 × 20 km area around each site to construct the time series used for calibration and validation. While this spatial scale is likely appropriate for the relatively homogeneous waters surrounding BOUSSOLE, it may encompass substantially different optical water types at the more heterogeneous AAOT site, potentially affecting the representativeness of the satellite-derived observations. Moreover, satellite-derived variables such as Chl represent spatially integrated surface properties, whereas the model explicitly resolves their vertical distribution. We reduced this scale mismatch by comparing satellite-derived variables with modelled concentrations averaged over the first optical depth, but differences in spatial and vertical sampling remain a source of uncertainty.

Additional uncertainty arises from the choices in how the spectral information is represented and selected for calibration. Previous ocean-colour studies have shown that different spectral bands and band combinations carry different information about phytoplankton and other optically active constituents (e.g., IOCCG, 2020; Wolanin et al., 2016). In model assimilation frameworks, the use of $R_{RS}(\lambda)$ directly rather than derived products has also been shown to provide a more direct link between observations and biogeochemical models (Jones et al., 2016). However, the extent to which the selection of individual $R_{RS}(\lambda)$ wavelengths, their weighting, or transformations affect parameter identifiability in coupled optical–biogeochemical model calibration remains comparatively less explored. All these pre-processing and representation choices should therefore be considered as additional sources of uncertainty and should be considered when interpreting the resulting parameter estimates and model improvements.

Despite these limitations, our results demonstrate that integrating $R_{RS}(\lambda)$ observations directly into coupled optical–biogeochemical models can improve the representation of ocean-colour properties and, at least in open ocean conditions, transfer these improvements to the simulated biogeochemical state, which is in agreement with the results of previous studies (Jones et al., 2016). By establishing a closer connection between what satellites observe and what ecosystem models simulate, direct assimilation of spectral $R_{RS}(\lambda)$ reduces the reliance on intermediate retrieval algorithms and creates new opportunities to link ocean-colour observations with ecosystem and carbon-cycle dynamics. In open-ocean waters, the information contained in $R_{RS}(\lambda)$ can constrain biogeochemical properties and processes, including phytoplankton biomass and community composition, while simultaneously informing the optical properties that mediate the link between the biological state and the observed $R_{RS}(\lambda)$.

In highly turbid coastal waters, however, the strong optical contribution of suspended particulate matter can limit the extent to which information on the phytoplankton state can be extracted from $R_{RS}(\lambda)$ alone. In these systems, improving the representation of $R_{RS}(\lambda)$ may primarily require accurate characterisation of the optical properties of non-algal particles, while improvements in phytoplankton biomass and carbon remain more difficult to achieve. Importantly, this limitation suggests a

https://doi.org/10.5194/egusphere-2026-6687
Preprint. Discussion started: 5 November 2026
© Author(s) 2026. CC BY 4.0 License.

complementary value of integrating $R_{RS}(\lambda)$ into biogeochemical models. Rather than serving only as a target for parameter calibration, $R_{RS}(\lambda)$ can be used as a diagnostic of model structure: where optical–biogeochemical mismatches persist, they can reveal whether discrepancies arise from poorly constrained parameters or from missing or oversimplified processes and optical representations. Our results suggest that the integration of $R_{RS}(\lambda)$ into marine ecosystem modelling might serve a dual purpose: improving model calibration and providing a framework for diagnosing structural deficiencies in the representation of the coupled optical and biogeochemical system.

This study was motivated by the increasing availability of multispectral sensors that allow determinations of $R_{RS}(\lambda)$ over the visible spectrum, the need for operationally available $R_{RS}(\lambda)$ products and the growing opportunity to establish a transparent and bidirectional pathway of information exchange between observations and models. Integrating radiative transfer models, coupled biogeochemical models, and advanced calibration approaches provides a framework in which ocean-colour observations can both constrain model parameters and reveal limitations in the representation of optical–biogeochemical interactions. Hyperspectral observations may further increase the information available to constrain these coupled models, and provide independent spectral information that helps disentangle the contributions of different optically active components. Developing consistent pathways for transferring information between ocean-colour observations and biogeochemical processes will be particularly relevant for exploiting the capabilities of current and forthcoming hyperspectral missions, potentially enabling improved discrimination of optical components and the detection of subtle spectral signals. Ultimately, this bidirectional integration can strengthen the consistency between observations and models, improve the representation and prediction of ecosystem state and biogeochemical fluxes, and enhance our ability to monitor and anticipate ocean responses to climate variability and change.

https://doi.org/10.5194/egusphere-2026-6687
Preprint. Discussion started: 5 November 2026
© Author(s) 2026. CC BY 4.0 License.

Appendix A

This appendix provides the complete list of optical and biogeochemical parameters included in the sensitivity analysis (SA) described in the main text. The parameters are grouped according to the FABM-BFM model instance in which they are used, and the table indicates differences in parameter values between the BOUSSOLE and AAOT configurations. Parameters marked with an asterisk are specific to the AAOT setup.

Table A1: List of the BGC parameters in FABM/BFM that have been perturbed during sensitivity analysis. * indicate parameters only used in the AAOT setup. When the value of a parameter differs between BOUS and AAOT, both are shown separated by a colon. Text in bold highlight the 12 values optimized at BOUSSOLE and text in italic highlight the 12 values optimized at AAOT.

Parameter name	Value	Description	Unit
LS (model: light_spectral)			
SdomX1	0.0175	spectral slope acdom of X1c	nm^{-1}
X1coeff	0.015	acdom coeff of X1c at 450nm	$m^2\ mgC^{-1}$
SdomX2	0.0162	spectral slope acdom of X2c	nm^{-1}
X2coeff	0.015	acdom coeff of X2c at 450nm	$m^2\ mgC^{-1}$
SdomX3	**0.0196**:0.018	spectral slope acdom of X3c	nm^{-1}
X3coeff	**0.00546**:0.015	acdom coeff of X3c at 450nm	$m^2\ mgC^{-1}$
Sapar	0.013	spectral slope anap	nm^{-1}
aparcoeff	0.00058	anap coeff at 440nm	$m^2\ mgC^{-1}$
Sbpar	0.5	exponent bnap	-
bparcoeff	0.012	bnap coeff at 550nm	$m^2\ mgC^{-1}$
bb_to_b	0.005	backscattering to total scattering ratio for R6	-
epsP1	0.0152	mean absorption coefficient from 400-700nm for P1	$m^2\ mgChl^{-1}$
epsP2	**0.0439**:0.0293	mean absorption coefficient from 400-700nm for P2	$m^2\ mgChl^{-1}$
epsP3	0.0443	mean absorption coefficient from 400-700nm for P3	$m^2\ mgChl^{-1}$
epsP4	0.0178	mean absorption coefficient from 400-700nm for P4	$m^2\ mgChl^{-1}$
bpsP1	0.014	mean scattering coefficient from 400-700nm for P1	$m^2\ mgChl^{-1}$
bpsP2	0.0077	mean scattering coefficient from 400-700nm for P2	$m^2\ mgChl^{-1}$
bpsP3	**0.0187**:0.0101	mean scattering coefficient from 400-700nm for P3	$m^2\ mgChl^{-1}$
bpsP4	0.0112	mean scattering coefficient from 400-700nm for P4	$m^2\ mgChl^{-1}$
bbrP1	0.002	backscattering to total scattering ratio for P1	-
bbrP2	0.0071	backscattering to total scattering ratio for P2	-
bbrP3	**0.0033**:0.0039	backscattering to total scattering ratio for P3	-
bbrP4	0.003	backscattering to total scattering ratio for P4	-
spmc1*	*0.00102525*	basal absorption at long wavelengths	$m^2\ g^{-1}$
spmc2*	*0.0240401*	specific absorption at 440nm	$m^2\ g^{-1}$
spmS*	*0.012862*	slope for exponential decline of aSPM with wavelength	nm^{-1}
spmb*	0.196469	specific scattering at 555nm	$m^2\ g^{-1}$
spmbb*	*0.00477547*	specific backscattering at 555nm	$m^2\ g^{-1}$
R6 (model: bfm_pelagic_base)			
rm	4.25	sinking velocity	$m\ d^{-1}$
P1/P2/P3/P4 (model: Phyto)			

https://doi.org/10.5194/egusphere-2026-6687
Preprint. Discussion started: 5 November 2026
© Author(s) 2026. CC BY 4.0 License.

q10	2/2.25/**1.025**:*1.998*/2	Q10 coefficient for temperature factor	-
temp	--/--/**0.66**:*0.84*/--	cut-off threshold for temperature factor	-
sum	2.5/2.6/3.5/1.5	maximum specific productivity at 10 degrees C	d^{-1}
srs	0.076/0.09/0.1/0.1	respiration rate at 10 degrees C	d^{-1}
sheo	--/--/--/100	half saturation constant for extra lysis	$mgC\ m^{-3}$
pu_ea	0.1/0.15/0.15/0.2	excreted fraction of primary production	-
pu_ra	0.1/0.1/0.2/0.1	activity respiration fraction	-
qun	0.025/0.025/0.025/0.025	membrane affinity for N	$m^3\ mgC^{-1}\ d^{-1}$
lN4	1/0.5/0.1/1	half-saturation constant for NH4 uptake preference over NO3	$mmolN\ m^{-3}$
qnlc	0.00687/0.00687/0.00687/0.00687	minimum N to C ratio	$mmolN\ mgC^{-1}$
qncPPY	0.0126/0.0126/0.0126/0.0126	reference quotum N:C	$mmolN\ mgC^{-1}$
xqn	2/2/2/2	multiplication factor for luxury storage	-
qup	0.0025/0.0035/0.0025/0.0025	membrane affinity for P	$m^3\ mgC\text{-}1\ d^{-1}$
qplc	0.00057/0.000352/0.00043:*0.000497*/0.00043	minimum P to C ratio	$mmolN\ mgC^{-1}$
qpcPPY	0.000786/0.000556/0.00072:*0.000655*/0.000556	reference quotum P:C	$mmolP\ mgC^{-1}$
xqp	2/2/2/2	multiplication factor for luxury storage	-
chPs	0.3/--/--/--	half saturation concentration for DSi limitation	$mmolSi\ m^{-3}$
qus	0.0025/--/--/--	membrane affinity for Si	$m^3\ mgC^{-1}\ d^{-1}$
qslc	0.007/--/--/--	minimum Si to C ratio	$mmolSi\ mgC^{-1}$
esNI	0.7/0.75/0.75/0.75	nutrient stress threshold for sinking	-
res	5/0/0/2.5	maximum sinking velocity	$m\ d^{-1}$
caco3r	--/0.3/--/--	reference PIC:POC (rain) ratio	-
fX2p	0.08/0.043/0.039/0.053	fraction of colored semi-labile DOC	-
sdchl	0.2/0.2/0.2/0.2	specific turnover rate for Chl	d^{-1}
QY	0.00075/0.000198/0.00099/0.000257	photochemical efficiency	$mgC\ uE^{-1}$
qlcPPY	0.026/**0.0497**:*0.0137*/0.014/0.019	reference quotum Chl:C	$mgChl\ mgC^{-1}$
epsChla	0.03/0.03/0.03/0.03	Chl-specific extinction coefficient	$m^2\ mgChl^{-1}$
B1 (model: PelBac)			
q10	2.95	Q10 value for temperature dependency	-
chdo	30	half-saturation constant for O2 limitation	$mmolO_2\ m^{-3}$
suhR1	0.5	specific potential uptake for nutrient-rich DOM	d^{-1}
suR2	0.05	specific potential uptake for semi-labile DOC	d^{-1}
suR6	0.1	specific potential uptake for POM	d^{-1}
sum	8.38	potential specific growth rate	d^{-1}
pu_ra	**0.9956**:*0.9999*	activity respiration fraction	-
pu_ra_o	0.2	additional respiration fraction at low O2 conc	-
srs	0.01	specific rest respiration	d^{-1}
qncPBA	0.017	optimal N to C ratio	$mmolN\ mgC^{-1}$
qpcPBA	0.0019	optimal P to C ratio	$mmolN\ mgC^{-1}$
qlnc	0.0085	minimal N to C ratio	$mmolN\ mgC^{-1}$
qlpc	0.00095	minimal P to C ratio	$mmolN\ mgC^{-1}$
qun	0.05	membrane affinity for N	$mmolN\ mgC^{-1}\ d^{-1}$
qup	0.005	membrane affinity for P	$mmolP\ mgC^{-1}\ d^{-1}$
chn	0.05	half saturation ammonium conc. for uptake	$mmolN\ m^{-3}$
chp	1	half saturation phosphate conc. for uptake	$mmolN\ m^{-3}$
rec	1	relaxation timescale for semi-labile excretion	d^{-1}
ruen	1	relaxation timescale for N uptake/remin.	d^{-1}

https://doi.org/10.5194/egusphere-2026-6687
Preprint. Discussion started: 5 November 2026
© Author(s) 2026. CC BY 4.0 License.

ruep	1	relaxation timescale for P uptake/remin.	d^{-1}
qro	0.5	stoichiometric coefficient for anaerobic reactions	$mmolHS^{-}\ mmolO2^{-1}$
pe_R1c	0.6	fractional content of C in cytoplasm	-
pe_R1n	0.72	fractional content of N in cytoplasm	-
pe_R1p	0.832	fractional content of P in cytoplasm	-
fX2b	0.02	fraction of colored semi-labile DOC	-
fX3b	0.018	fraction of colored semi-refractory DOC	-
Z5/Z6 (model: MicroZoo)			
q10	2/2	Q10 coefficient for temperature factor	-
srs	0.02/0.02	respiration rate at 10 degrees C	d^{-1}
sum	**5.15**:2.71/3.88	potential growth rate	d^{-1}
sdo	0.05/0.05	mortality rate due to oxygen limitation	d^{-1}
pu	**0.505**:*0.355*/0.3	assimilation efficiency	-
pu_ea	**0.467**:*0.356*/0.4	fraction of activity excretion	-
chro	8/8	half-saturation oxygen concentration	$mmolO_2\ m^{-3}$
chuc	30/100	half-saturation food concentration for Type II	$mgC\ m^{-3}$
minfood	50/50	half-saturation food concentration for preference factor	$mgC\ m^{-3}$
pecaco3	0.5/0.5	portion of egested calcified shells during grazing	-
qpcMIZ	0.00185/0.00185	maximum quotum P:C	$mmolN\ mgC^{-1}$
qncMIZ	0.0167/0.0167	maximum quotum N:C	$mmolN\ mgC^{-1}$
suprey1	0.1/1	availability of pelagic Bacteria group B1	-
suprey2	0.7/0	availability of phytoplankton group P1	-
suprey3	1/0.2	availability of phytoplankton group P2	-
suprey4	0.1/1	availability of phytoplankton group P3	-
suprey5	0.1/0	availability of phytoplankton group P4	-
suprey6	1/0	availability of microzooplankton group Z5	-
suprey7	1/0.2	availability of microzooplankton group Z6	-
pe_R1c	0.6/0.6	fractional content of C in cytoplasm	-
pe_R1n	0.72/0.72	fractional content of N in cytoplasm	-
pe_R1p	0.832/0.832	fractional content of P in cytoplasm	-
fX1z	0.018/0.03	fraction of colored labile DOC in excretion	-
Z3/Z4 (model: MesoZoo)			
q10	2/2	Q10 value for physiological rates	-
srs	0.01/0.02	respiration rate at 10 degrees C	d^{-1}
sum	2/2	maximal productivity at 10 degrees C	d^{-1}
sd	0.02/0.02	background natural mortality	d^{-1}
vum	0.008/0.02	specific search volume	$m^3\ mgC^{-1}\ d^{-1}$
puI	0.6/0.6	assimilation efficiency	-
peI	0.3/0.35	fraction of faeces production	-
sdo	0.01/0.01	specific density-dependent mortality	$m^3\ mgC^{-1}\ d^{-1}$
sds	2/2	exponent of density-dependent mortality	-
pecaco3	0.75/0.75	portion of egested calcified shells during grazing	-
qpcMEZ	0.00167/0.00167	maximum quotum P:C	$mmolP\ mgC^{-1}$
qncMEZ	0.015/0.015	maximum quotum N:C	$mmolP\ mgC^{-1}$
clO2o	30/30	half-saturation oxygen concentration	$mmolO2\ m^{-3}$
suprey1	--/1	availability of phytoplankton group P1	-
suprey2	--/0.75	availability of phytoplankton group P2	-

https://doi.org/10.5194/egusphere-2026-6687
Preprint. Discussion started: 5 November 2026
© Author(s) 2026. CC BY 4.0 License.

suprey3	1/1	availability of phytoplankton group P4	-
suprey4	--/1	availability of microzooplankton group Z5	-
suprey5	1/1	availability of microzooplankton group Z4	-
suprey6	1/--	availability of microzooplankton group Z3	-
PC (model: PelChem)			
clO2o	10	half-saturation O_2 concentration for nitrif. and reoxidation	$mmolO_2\ m^{-3}$
clN6r	1	half-saturation concentration of reduction equivalents for denitrif.	$mmolO_2\ m^{-3}$
sN4N3	0.01	specific nitrification rate at 10 degrees C	d^{-1}
q10N4N3	2.367	Q10 factor for nitrification/denit.	-
qon_nitri	2	stoichiometric coefficient for nitrification	$mmolO_2\ mmolN^{-1}$
qro	0.5	stoichiometric coefficient for anaerobic reactions	$mmolO_2\ mmolN^{-1}$
sN3O4n	0.35	specific denitrification rate	d^{-1}
rPAo	1	reference anoxic mineralization rate	$mmolO_2\ m^{-3}\ d^{-1}$
qon_dentri	1.25	stoichiometric coefficient for denitrification	$mmolO_2\ mmolN^{-1}$
rOS	0.05	specific reoxidation rate of reduction equivalents	d^{-1}
sR6N5	0.1	specific remineralization rate of biogenic silica	d^{-1}
q10R6N5	1.49	Q10 factor for biogenic silica	-
bX1c	0.167	photodegradation (bleaching) rate X1c	d^{-1}
bX2c	0.167	photodegradation (bleaching) rate X2c	d^{-1}
bX3c	0.0338	photodegradation (bleaching) rate X3c	d^{-1}
IX1	60	light threshold for X1c bleaching	$\mu E\ m^{-2}\ s^{-1}$
IX2	60	light threshold for X2c bleaching	$\mu E\ m^{-2}\ s^{-1}$
IX3	760	light threshold for X3c bleaching	$\mu E\ m^{-2}\ s^{-1}$
rX3c	0.00003	remineralization rate X3c and R3c	d^{-1}
q10X	2.95	Q10 for CDOM degradation	-
TauC	0:1	remineralization of C in detritus	d^{-1}
TauN	0:0.5	remineralization of N in detritus	d^{-1}
TauP	0:1	remineralization of P in detritus	d^{-1}
Amm_rem	0:0.2	fraction of detritus remineralized to NH4	-
O5 (model: CalciteDissolution)			
kdca	10.9	calcite dissolution rate constant	d^{-1}
nomega	1	order of the dissolution rate dependence on Omega	-
wsinkPIC	30	sinking velocity of PIC (Calcite)	$m\ d^{-1}$
c0	0.00001	background concentration	$mgC\ m^{-3}$

https://doi.org/10.5194/egusphere-2026-6687
Preprint. Discussion started: 5 November 2026
© Author(s) 2026. CC BY 4.0 License.

Appendix B

This appendix provides a complementary set of figures that completes the results regarding the optimization of parameter values (**Fig. B1** and **Fig. B2**), the simulation of the spectra (**Fig. B3**) and timeseries (**Fig. B4** and **Fig. B5**) of non-GA-used $R_{RS}(\lambda)$, the simulation of biogeochemical variables at the two sites (**Fig. B6** and **Fig. B7**), and the parameter trajectories during the targeted experiments at BOUSSOLE (**Fig. B8**) and at AAOT (**Fig. B9**).

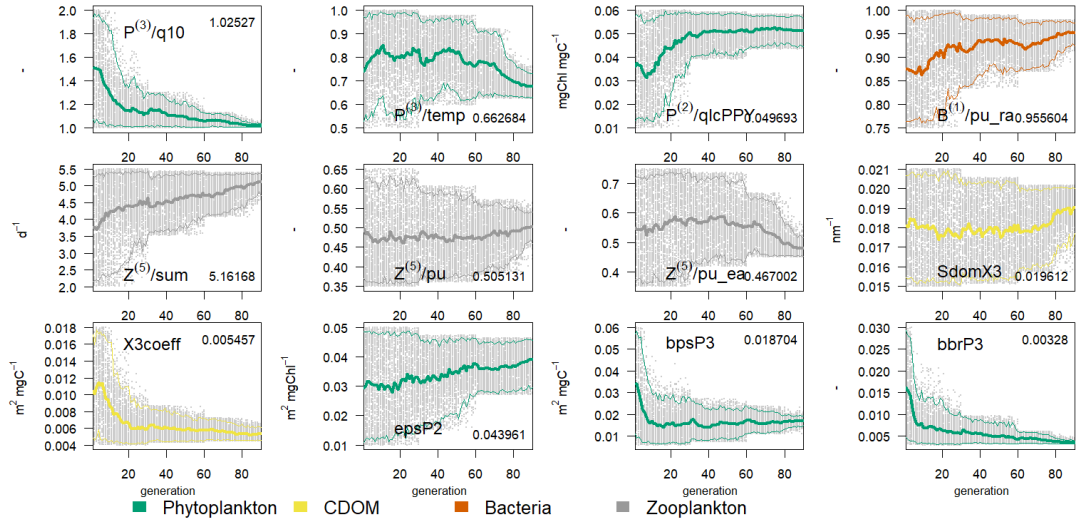


Figure B1: Optimization trajectories during GA of parameter values at the BOUSSOLE site, color-coded by FABM module. The rank order found by the SA is followed in row-order. Parameter labels, perturbed range of values and final values optimized are displayed in Table 2 of the main text.

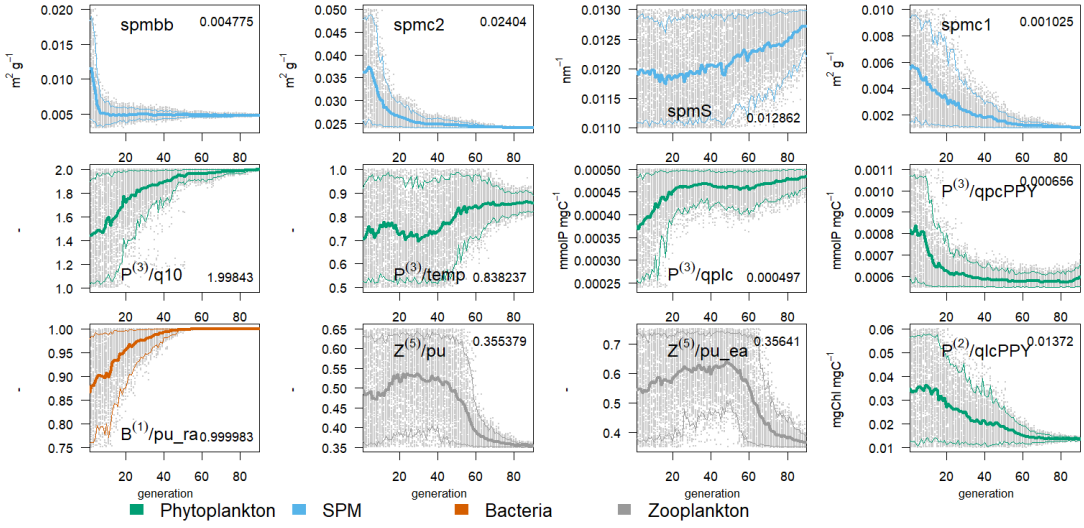


Figure B2: Optimization trajectories during GA of parameter values at the AAOT site, color-coded by FABM module. The rank order found by the SA is followed in row-order. Parameter labels, perturbed range of values and final values optimized are displayed in Table 3 of the main text.

https://doi.org/10.5194/egusphere-2026-6687
Preprint. Discussion started: 5 November 2026
© Author(s) 2026. CC BY 4.0 License.

For BOUSSOLE, the simulated $R_{RS}(\lambda)$ spectra (in blue in **Fig. B3**) aligns with the MULTI-sensor product (black dots) relatively well, with some deviations from April to May. Overall, the model reproduces $R_{RS}(\lambda)$ spectra peaked at 400 nm and with larger differences between short and long wavelengths (larger spectral slopes) between May and October. For AAOT, the model overestimates $R_{RS}(\lambda)$ (in orange in **Fig. B3**) between 450 and 575 nm from April to September compared to the MULTI-sensor product (black triangles), and underestimates $R_{RS}(\lambda)$ in the same spectral range from November to March. Therefore, although the model reproduces the $R_{RS}(\lambda)$ spectra peaked at 500-525 nm throughout the year and with larger differences between short and long wavelengths (larger spectral slopes) in the winter months, it does not fully capture the differences in amplitude between winter and summer observed at this site.

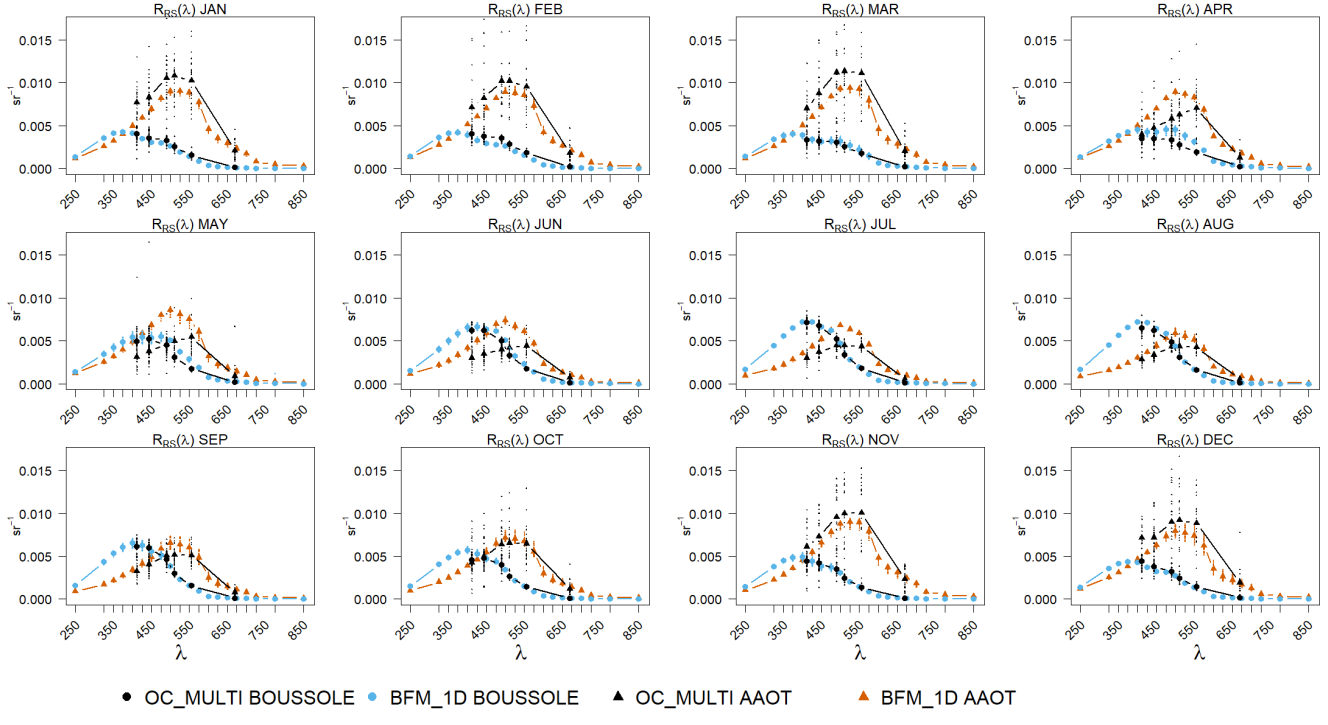


Figure B3: Four-years average of $R_{RS}(\lambda)$ at BOUSSOLE (2017-2020) and AAOT (2014-2017) from CMS MULTI-sensor (black) and OLCI-sensor (grey), and from the optimized model output at BOUSSOLE (blue) and AAOT (orange).

https://doi.org/10.5194/egusphere-2026-6687
Preprint. Discussion started: 5 November 2026
© Author(s) 2026. CC BY 4.0 License.

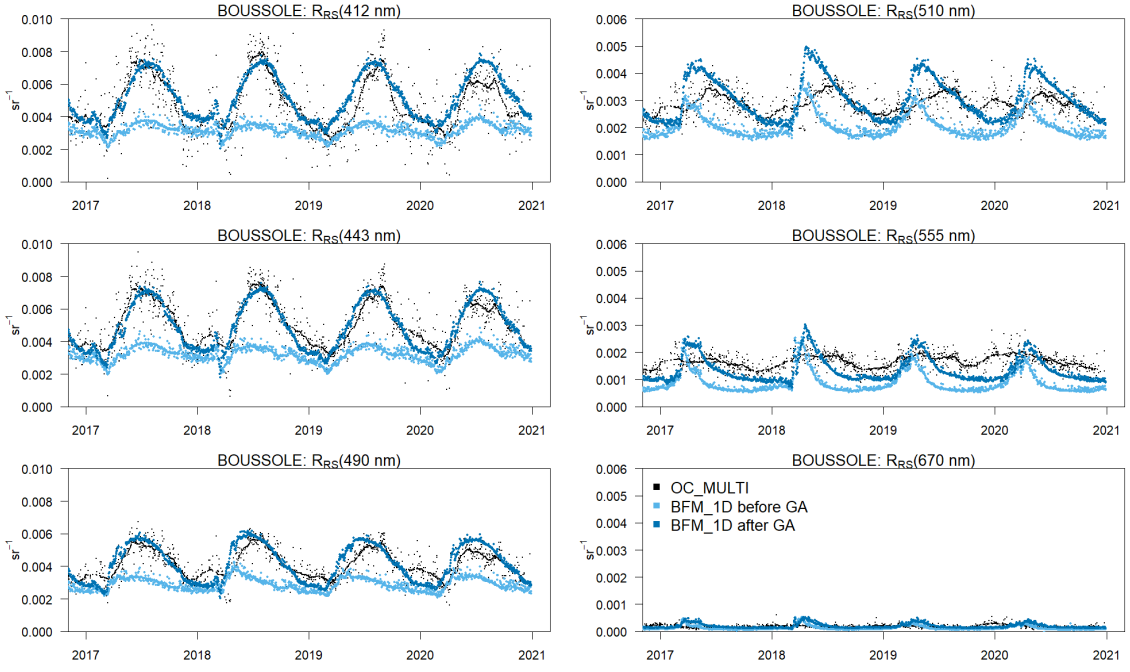


Figure B4: Timeseries of CMS MULTI-sensor $R_{RS}(\lambda)$ (black) compared to initial (light blue) and $R_{RS}(\lambda)$-calibrated with GA (dark blue) model simulations at BOUSSOLE. Note that the y-axis scales are different between right and left panels.

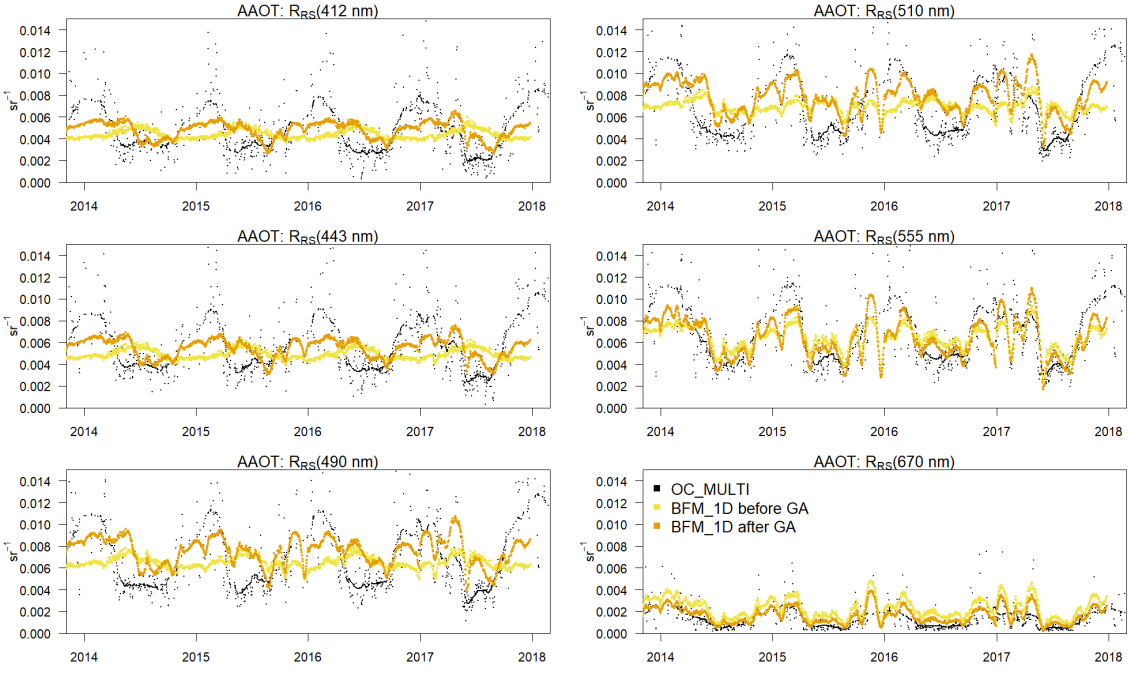


Figure B5: Timeseries of CMS MULTI-sensor $R_{RS}(\lambda)$ (black) compared to initial (yellow) and $R_{RS}(\lambda)$-calibrated with GA (orange) model simulations at AAOT. Note that the y-axis scales are equal.

https://doi.org/10.5194/egusphere-2026-6687
Preprint. Discussion started: 5 November 2026
© Author(s) 2026. CC BY 4.0 License.

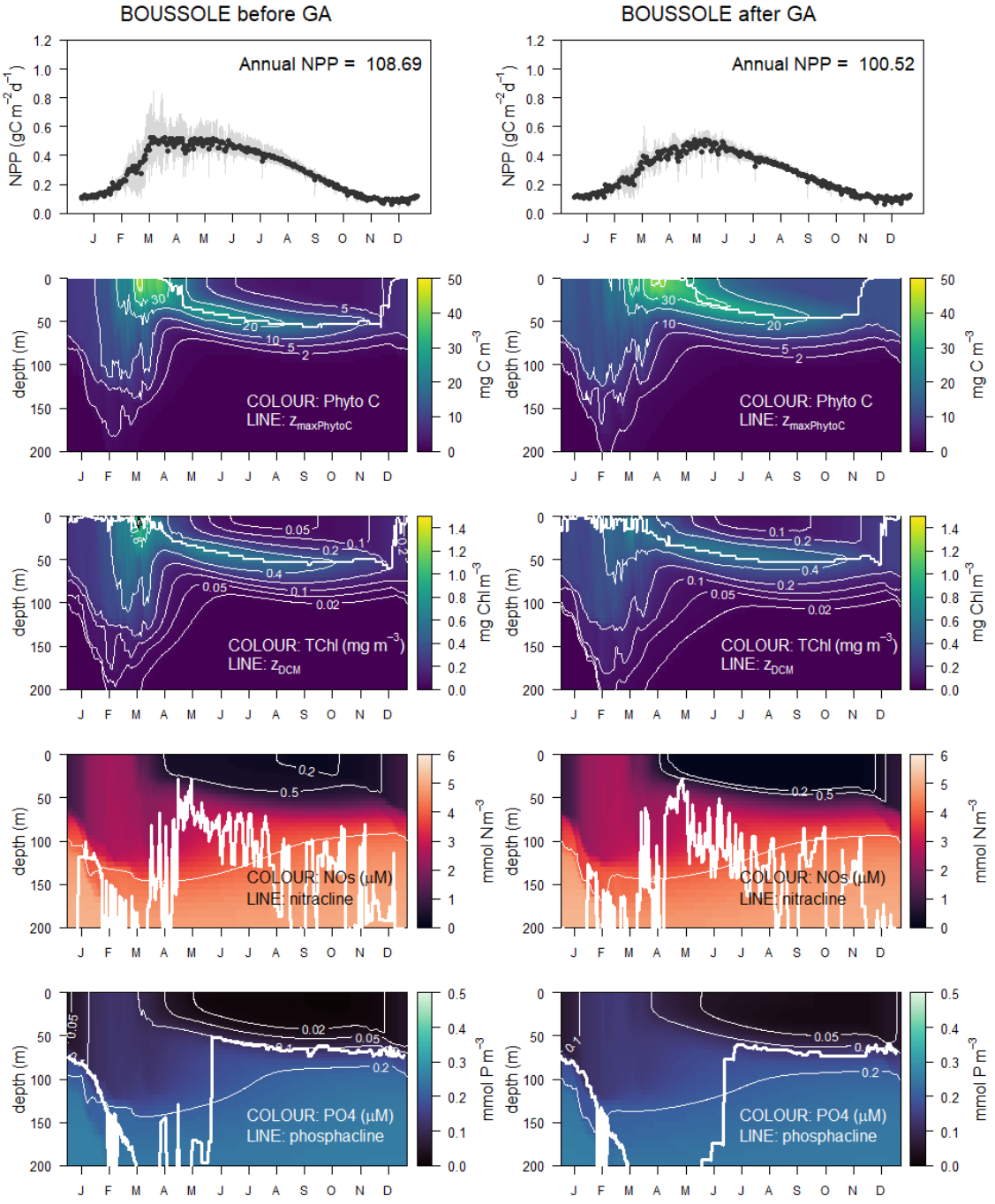
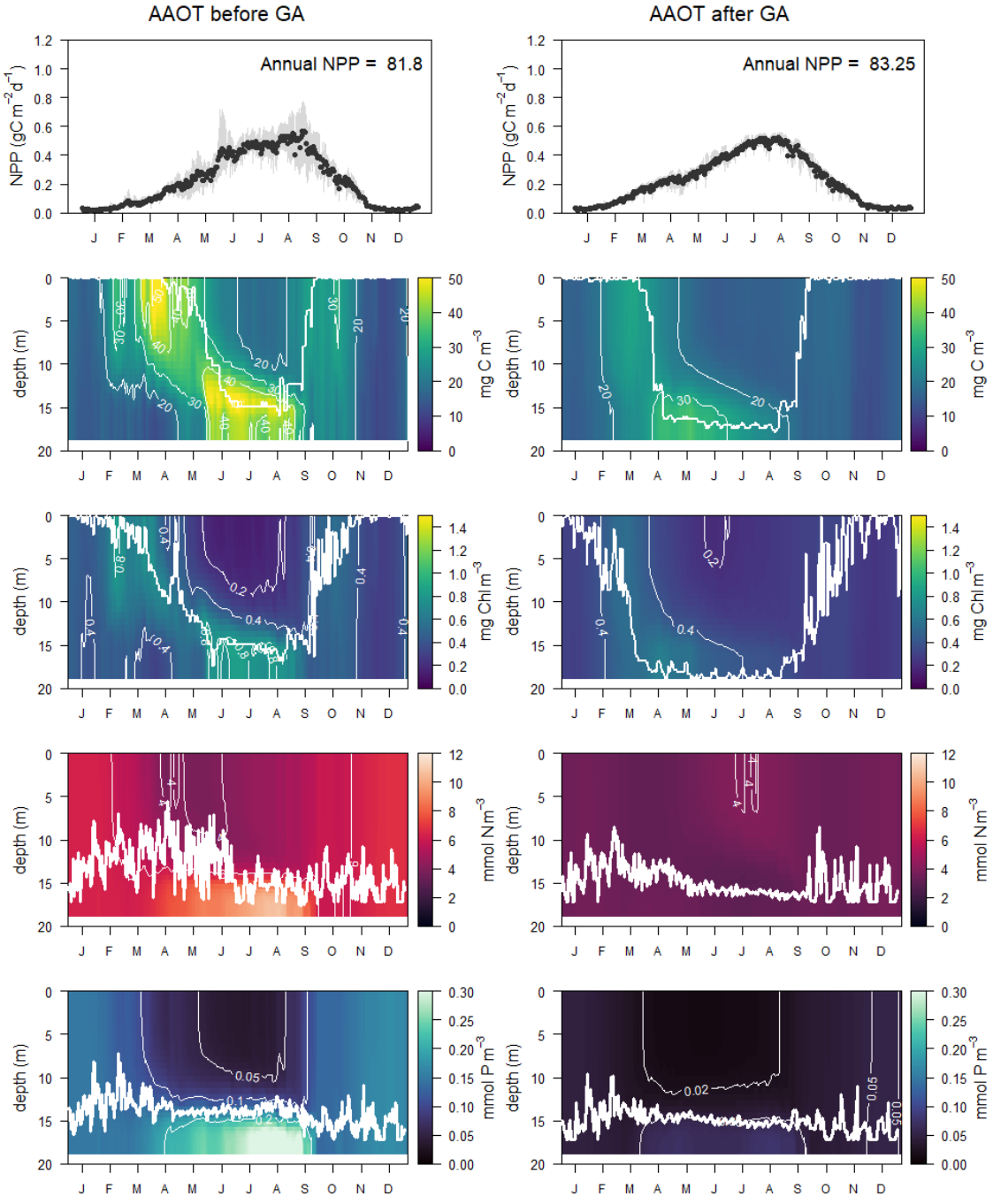


Figure B6: Annual average (2017-2020) evolution at the BOUSSOLE site of the vertically integrated NPP (0-200m), and profiles of phytoplankton C, total Chl (mg m^{-3}), DIN and DIP (mmol m^{-3}) in the simulations before GA optimization (left panels) and afterwards (right panels). The thick white lines in the profiles show the depth where the concentration of phytoplankton C and Chl is maximum, the depth of the nitracline and the phosphacline with a threshold criterium of 0.08 and 0.02 (Pujo-Pay et al., 2011), respectively.

https://doi.org/10.5194/egusphere-2026-6687
Preprint. Discussion started: 5 November 2026
© Author(s) 2026. CC BY 4.0 License.



745 **Figure B7: Annual average (2014-2017) evolution at the AAOT site of the vertically integrated NPP (full column), and profiles of phytoplankton C, total Chl, DIN and DIP in the simulations before GA optimization (left panels) and afterwards (right panels). The position of the panels is the same as in Fig. B7. The thick white lines in the profiles show the depth where the concentration of phytoplankton C and Chl is maximum, the depth of the nitracline and the phosphacline with a threshold criterium of 0.08 and 0.02 (Pujo-Pay et al., 2011), respectively.**

https://doi.org/10.5194/egusphere-2026-6687
Preprint. Discussion started: 5 November 2026
© Author(s) 2026. CC BY 4.0 License.

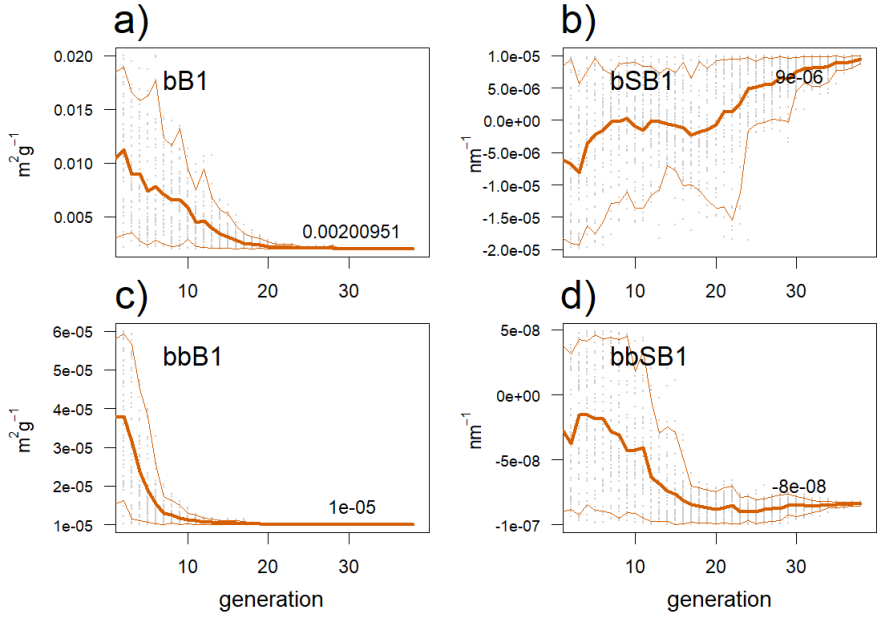


Figure B8: Optimization trajectories of bacteria ($B^{(1)}_C$, mg m^{-3}) scattering parameter values: the mass-specific scattering (bB1) and backscattering (bbB1) coefficients at 555 nm and their (bSB1 and bbSB1, respectively) spectral slopes around 555 nm during the targeted GA experiment at the BOUSSOLE site.

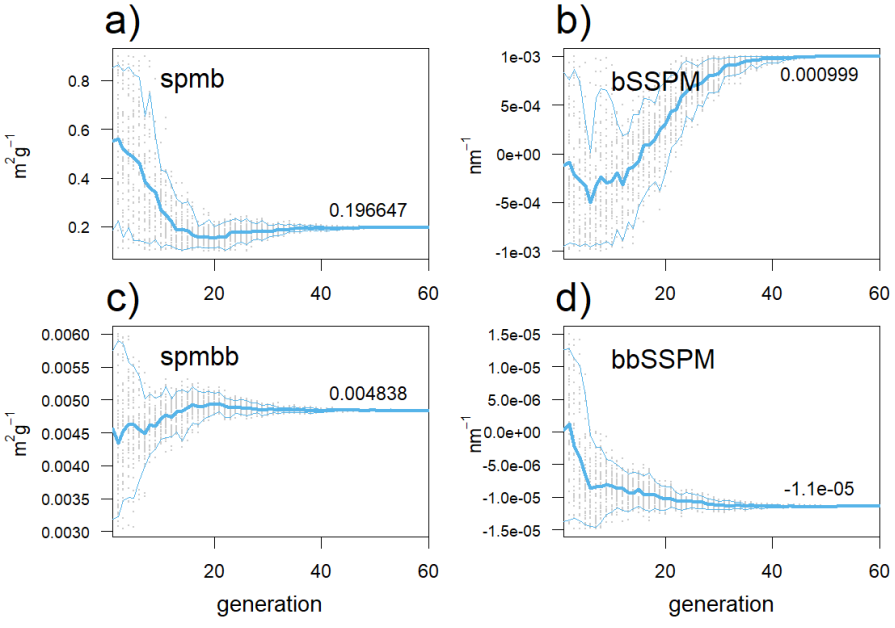


Figure B9: Optimization trajectories of SPM (g m^{-3}) scattering parameter values: the mass-specific scattering (spmb) and backscattering (spmbb) coefficients at 555 nm and their (bSSPM and bbSSPM, respectively) spectral slopes around 555 nm during the targeted GA experiment at the AAOT site.

https://doi.org/10.5194/egusphere-2026-6687
Preprint. Discussion started: 5 November 2026
© Author(s) 2026. CC BY 4.0 License.

Code availability

The GOTM code is available at https://www.github.com/gotm-model. FABM code is available at https://github.com/fabm-model/fabm.git. ParSAC code is available at https://doi.org/10.5281/zenodo.4276111. The BFM code adapted to work under the FABM convention is available at https://github.com/inogs/bfmforfabm.git and the bio-optical model in https://github.com/BIOPTIMOD/Forward_Adjoint.git. The SEAMLESS prototype that bundles all five tools and includes instructions for installation is available at https://github.com/BoldingBruggeman/seamless-notebooks. The 1D setups created specifically for this study are available from https://github.com/ealvarez-s/setup_BFM1D_BOUSSOLE.git for BOUSSOLE and from https://github.com/ealvarez-s/setup_BFM1D_AcquaAlta.git for AAOT. The repository for each site contains the meteorological forcing files (ERA5,) and the vertical profiles of T/S and BGC variables extracted from the Mediterranean BGC Reanalysis (Cossarini et al., 2021) and the CADEAU model (Bruschi et al., 2021), respectively.

Data availability

This study has been conducted using mostly OC-based product OCEANCOLOUR_MED_BGC_L3_MY from the E.U. Copernicus Marine Service Information: https://doi.org/10.48670/moi-00299.

The SPM Ifremer product have been obtained from the ftp://ftp.ifremer.fr/ifremer/cersat/products/gridded/ocean-color/atlantic/EUR-L4-SPIM-ATL-v01/ (accessed as guest 22/11/2021).

Phytoplankton carbon concentrations have been obtained from the Carbon-based Productivity Model (CbPM) webpage as 8-day composites in the 2160 by 4320 grid from MODIS (https://orca.science.oregonstate.edu/2160.by.4320.8day.hdf.carbon2.m.php, last accessed 23/10/2025) and from VIIRS (https://orca.science.oregonstate.edu/2160.by.4320.8day.hdf.carbon2.v.php, last accessed 23/10/2025).

The near-surface marine $b_{bp}(\lambda)$ data at AAOT has been obtained from the CoASTS-BiOMaP data set (Zibordi and Berthon, 2024) available at PANGAEA: https://doi.org/10.1594/PANGAEA.971945.

The BOUSSOLE field-data used in this study comprises the gridded product of temperature and salinity at DYFAMED obtained from the OceanSITES Global Data Assembly Center via ftp (ftp://ftp.ifremer.fr/ifremer/oceansites, accessed 22/11/2021) and the Chl concentrations that were obtained from https://boussole.imev-mer.fr/html/boussole_data/other_useful_files.php.html (accessed 16/01/2024). At the time of publication, BOUSSOLE Chl is also available at SeaBASS: https://doi.org/10.5067/SeaBASS/BOUSSOLE/DATA001.

The AAOT field-data used in this study comprises concentrations of Chl and nano- plus micro-phytoplankton biomass above 6.5m depth for the period 2014-2017, both timeseries will be deposited in a FAIR-aligned data repository at the time of eventual publication.

https://doi.org/10.5194/egusphere-2026-6687
Preprint. Discussion started: 5 November 2026
© Author(s) 2026. CC BY 4.0 License.

Author contributions

EÁ, GC and PL conceptualized the research. EÁ, GO and PL developed the methodology. FBA and FA contributed with radiometric and biogeochemical data at AAOT. EÁ performed the simulations, did the data analysis and wrote the original draft. All co-authors reviewed, edited, and approved the final manuscript. GC and PL provided supervision and funding through the NECCTON project.

Competing interests

The authors declare they do not have any competing interest that might have influenced the results of this work.

Acknowledgements

This work has been supported by the NECCTON project, funded by the European Union's Horizon Europe research and innovation programme under grant agreement No 101081273. The development of the SEAMLESS prototype that integrates GOTM, FABM, BFM and ParSAC has been funded by the European Union's Horizon 2020 research and innovation programme under grant agreement No 101004032. The numerical simulations were conducted on the GALILEO100 supercomputing facility at the CINECA consortium; we acknowledge CINECA for providing high-performance computing resources and support. The BOUSSOLE project was funded by the Centre National d'Etudes Spatiales (CNES) and the European Space Agency (ESA) and supported by the French Oceanographic Fleet. We do acknowledge that they make available data in the project webpage and in the SeaBASS portal. The Acqua Alta Oceanographic Platform (AAOT) contributes to the European research infrastructures LTER in the Italian (LTER-Italy), European (LTER-Europe), and International (LTER-International) Long-Term Ecological Research (LTER) networks. The time series analyzed in this article were collected within the context of these networks. The authors wish to thank Francesco Acri and Stefania Finotto for chlorophyll and phytoplankton analyses, respectively.

https://doi.org/10.5194/egusphere-2026-6687
Preprint. Discussion started: 5 November 2026
© Author(s) 2026. CC BY 4.0 License.

References

Aas, E.: Two-stream irradiance model for deep waters, Appl. Optics, 26, 2095–2101, https://doi.org/10.1364/AO.26.002095, 1987.

Ackleson, S. G., Balch, W. M., and Holligan, P. M.: Response of water-leaving radiance to particulate calcite and chlorophyll a concentrations: a model for Gulf of Maine coccolithophore blooms, J. Geophys. Res., 99, 7483–7500, https://doi.org/10.1029/93JC02150, 1994.

Álvarez, E., Lazzari, P., and Cossarini, G.: Phytoplankton diversity emerging from chromatic adaptation and competition for light, Prog. Oceanogr., 204, 102789, https://doi.org/10.1016/j.pocean.2022.102789, 2022.

Álvarez, E., Cossarini, G., Teruzzi, A., Bruggeman, J., Bolding, K., Ciavatta, S., Vellucci, V., D'Ortenzio, F., Antoine, D., and Lazzari, P.: Chromophoric dissolved organic matter dynamics revealed through the optimization of a spectrally and vertically resolved model in the NW Mediterranean Sea, Biogeosciences, 20, 4591–4624, https://doi.org/10.5194/bg-20-4591-2023, 2023.

Antoine, D. and Vellucci, V.: BOUSSOLE project: HPLC dataset, https://boussole.imev-mer.fr/html/boussole_data/other_useful_files.php.html, last access: 1 September 2026, 2024., 2024.

Babin, M., Morel, A., Fournier-Sicre, V., Fell, F., and Stramski, D.: Light scattering properties of marine particles in coastal and open ocean waters as related to the particle mass concentration, Limnol. Oceanogr., 48, 843–859, https://doi.org/10.4319/lo.2003.48.2.0843, 2003a.

Babin, M., Stramski, D., Ferrari, G. M., Claustre, H., Bricaud, A., Obolensky, G., and Hoepffner, N.: Variations in the light absorption coefficients of phytoplankton, nonalgal particles, and dissolved organic matter in coastal waters around Europe, J. Geophys. Res. Oceans, 108, https://doi.org/10.1029/2001JC000882, 2003b.

Baird, M. E., Cherukuru, N., Jones, E., Margvelashvili, N., Mongin, M., Oubelkheir, K., Ralph, P. J., Rizwi, F., Robson, B. J., Schroeder, T., Skerratt, J., Steven, A. D. L., and Wild-Allen, K. A.: Remote-sensing reflectance and true colour produced by a coupled hydrodynamic, optical, sediment, biogeochemical model of the Great Barrier Reef, Australia: Comparison with satellite data, Environ Modell Softw, 78, 79–96, https://doi.org/10.1016/j.envsoft.2015.11.025, 2016.

Berthon, J.-F. and Zibordi, G.: Bio-optical relationships for the northern Adriatic Sea, Int. J. Remote Sens., 25, 1527–1532, https://doi.org/10.1080/01431160310001592544, 2004.

Bruggeman, J. and Bolding, K.: A general framework for aquatic biogeochemical models, Environ Modell Softw, 61, 249–265, https://doi.org/10.1016/j.envsoft.2014.04.002, 2014.

Bruggeman, J. and Bolding, K.: parsac: parallel sensitivity analysis and calibration (0.5.7), https://doi.org/10.5281/zenodo.4280520, 2020., 2020.

https://doi.org/10.5194/egusphere-2026-6687
Preprint. Discussion started: 5 November 2026
© Author(s) 2026. CC BY 4.0 License.

Bruggeman, J., Bolding, K., Nerger, L., Teruzzi, A., Spada, S., Skákala, J., and Ciavatta, S.: EAT v1.0.0: a 1D test bed for physical–biogeochemical data assimilation in natural waters, Geosci. Model Dev., 17, 5619–5639, https://doi.org/10.5194/gmd-17-5619-2024, 2024.

Bruschi, A., Lisi, I., De Angelis, R., Querin, S., Cossarini, G., Di Biagio, V., Salon, S., Solidoro, C., Fassina, D., Ancona, S., and Silvestri, C.: Indexes for the assessment of bacterial pollution in bathing waters from point sources: The northern Adriatic Sea CADEAU service, J. Environ. Manage., 293, 112878, https://doi.org/10.1016/j.jenvman.2021.112878, 2021.

Burchard, H., Bolding, K., and Villarreal, M.: GOTM, a general ocean turbulence model: Theory, implementation and test cases. Report EUR 18745, 1999.

Ciavatta, S., Torres, R., Martinez-Vicente, V., Smyth, T., Dall'Olmo, G., Polimene, L., and Allen, J. I.: Assimilation of remotely-sensed optical properties to improve marine biogeochemistry modelling, Prog. Oceanogr., 127, 74–95, https://doi.org/10.1016/j.pocean.2014.06.002, 2014.

Coppini, G., Clementi, E., Cossarini, G., Salon, S., Korres, G., Ravdas, M., Lecci, R., Pistoia, J., Goglio, A. C., Drudi, M., Grandi, A., Aydogdu, A., Escudier, R., Cipollone, A., Lyubartsev, V., Mariani, A., Cretì, S., Palermo, F., Scuro, M., Masina, S., Pinardi, N., Navarra, A., Delrosso, D., Teruzzi, A., Di Biagio, V., Bolzon, G., Feudale, L., Coidessa, G., Amadio, C., Brosich, A., Miró, A., Alvarez, E., Lazzari, P., Solidoro, C., Oikonomou, C., and Zacharioudaki, A.: The Mediterranean Forecasting System – Part 1: Evolution and performance, Ocean Science, 19, 1483–1516, https://doi.org/10.5194/os-19-1483-2023, 2023.

Cossarini, G., Feudale, L., Teruzzi, A., Bolzon, G., Coidessa, G., Solidoro, C., Di Biagio, V., Amadio, C., Lazzari, P., Brosich, A., and Salon, S.: High-Resolution Reanalysis of the Mediterranean Sea Biogeochemistry (1999–2019), Front. Mar. Sci., 8, https://doi.org/10.3389/fmars.2021.741486, 2021.

Cossarini, G., Moore, A., Ciavatta, S., and Fennel, K.: Numerical models for monitoring and forecasting ocean biogeochemistry: a short description of present status, in: Ocean prediction: present status and state of the art (OPSR), vol. 5-opsr, edited by: Álvarez Fanjul, E., Ciliberti, S. A., Pearlman, J., Wilmer-Becker, K., and Behera, S., Copernicus Publications, https://doi.org/10.5194/sp-5-opsr-12-2025, 2025.

Davies, E. J., Basedow, S. L., and McKee, D.: The hidden influence of large particles on ocean colour, Sci. Rep., 11, 3999-undefined, https://doi.org/10.1038/s41598-021-83610-5, 2021.

Dutkiewicz, S., Hickman, A. E., Jahn, O., Gregg, W. W., Mouw, C. B., and Follows, M. J.: Capturing optically important constituents and properties in a marine biogeochemical and ecosystem model, Biogeosciences, 12, 4447–4481, https://doi.org/10.5194/bg-12-4447-2015, 2015.

E.U. Copernicus Marine Service Information: Mediterranean Sea, Bio-Geo-Chemical, L3, daily Satellite Observations (1997-ongoing), https://doi.org/10.48670/moi-00299, 2025., 2025.

https://doi.org/10.5194/egusphere-2026-6687
Preprint. Discussion started: 5 November 2026
© Author(s) 2026. CC BY 4.0 License.

Fettweis, M., Belliard, JP., Silori, S., Terseleer, N., Tran, D., Delhaye, L., Martinez, L. A., Brun, A., Sabbe, K., De Rijcke, M., Lee, B. J., Riethmüller, R., Shen, X., Verney, R., Ha, H. K., and Desmit, X.: Suspended particulate matter along the land–ocean continuum, Nat Rev Earth Environ, https://doi.org/https://doi.org/10.1038/s43017-026-00815-w, 2026.

Feudale, L., Bolzon, G., Lazzari, P., Salon, S., Teruzzi, A., Di Biagio, V., Coidessa, G., Álvarez, E., Amadio, C., and Cossarini, G.: Mediterranean Sea Biogeochemical Analysis and Forecast (CMS MED-Biogeochemistry, MedBFM4 System) (Version 1), https://doi.org/https://doi.org/10.48670/mds-00358, 2022., 2022.

Gallegos, C. L., Werdell, P. J., and McClain, C. R.: Long-term changes in light scattering in Chesapeake Bay inferred from Secchi depth, light attenuation, and remote sensing measurements, J Geophys Res-Oceans, 116, 1–19, https://doi.org/10.1029/2011JC007160, 2011.

Gohin, F.: Annual cycles of chlorophyll-a, non-algal suspended particulate matter, and turbidity observed from space and in-situ in coastal waters, Ocean Science, 7, 705–732, https://doi.org/10.5194/os-7-705-2011, 2011.

Gohin, F., Loyer, S., Lunven, M., Labry, C., Froidefond, J.-M., Delmas, D., Huret, M., and Herbland, A.: Satellite-derived parameters for biological modelling in coastal waters: Illustration over the eastern continental shelf of the Bay of Biscay, Remote Sens. Environ., 95, 29–46, https://doi.org/10.1016/j.rse.2004.11.007, 2005.

Golbol, M., Vellucci, V., and Antoine, D.: BOUSSOLE, https://doi.org/10.18142/1, 2000.

Gregg, W. W.: A Coupled Ocean–Atmosphere Radiative Model for Global Ocean Biogeochemical Model, NASA Technical Report Series on Global Modeling and Data Assimilation, NASA/TM- 2002-104606, 22, 2002.

Gregg, W. W. and Casey, N. W.: Skill assessment of a spectral ocean-atmosphere radiative model, J Marine Syst, 76, 49–63, https://doi.org/10.1016/j.jmarsys.2008.05.007, 2009.

Gregg, W. W. and Rousseaux, C. S.: Simulating PACE Global Ocean Radiances, Front Mar Sci, 4, 1–19, https://doi.org/10.3389/fmars.2017.00060, 2017.

Grégoire, M., Cossarini, G., Derval, C., Gutknecht, E., Kay, S., Lamouroux, J., Morrison, H., Perruche, C., Samuelsen, A., Spruch, L., Teruzzi, A., Vandenbulcke, L., Von Schuckmann, K., and Wakamatsu, T.: Review and Synthesis: operational prediction of ocean biogeochemistry in the Copernicus Marine Service. Main achievements and perspectives, https://doi.org/10.5194/egusphere-2026-813, 21 April 2026., 2026.

Hillebrand, H., Dürselen, C.-D., Kirschtel, D., Pollingher, U., and Zohary, T.: Biovolume Calculation for Pelagic and Benthic Microalgae, J Phycol, 35, 403–424, https://doi.org/10.1046/j.1529-8817.1999.3520403.x, 1999.

Holm-Hansen, O., Lorenzen, C. J., Holmes, R. W., and Strickland, J. D. H.: Fluorometric Determination of Chlorophyll, ICES Journal of Marine Science, 30, 3–15, https://doi.org/10.1093/icesjms/30.1.3, 1965.

IOCCG: Remote Sensing of Ocean Colour in Coastal, and Other Optically-Complex, Waters, Dartmouth, 2000.

https://doi.org/10.5194/egusphere-2026-6687
Preprint. Discussion started: 5 November 2026
© Author(s) 2026. CC BY 4.0 License.

IOCCG: Synergy between Ocean Colour and Biogeochemical/Ecosystem Models, edited by: Dutkiewicz, S., International Ocean-Colour Coordinating Group (IOCCG), Dartmouth, NS, Canada, 184-pp pp., https://doi.org/10.25607/OBP-711, 2020.

IOCCG: A Scientific Roadmap of Aquatic Hyperspectral Remote Sensing: Overview of Status, Challenges and Future Perspectives, Version 1.0., edited by: Bracher, A., Dogliotti, A. I., and Werdell, J., International Ocean-Colour Coordinating Group (IOCCG), Dartmouth, NS, Canada, 122 pp., https://doi.org/https://doi.org/10.25607/OBP-2062, 2026.

Jones, E. M., Baird, M. E., Mongin, M., Parslow, J., Skerratt, J., Lovell, J., Margvelashvili, N., Matear, R. J., Wild-Allen, K., Robson, B., Rizwi, F., Oke, P., King, E., Schroeder, T., Steven, A., and Taylor, J.: Use of remote-sensing reflectance to constrain a data assimilating marine biogeochemical model of the Great Barrier Reef, Biogeosciences, 13, 6441–6469, https://doi.org/10.5194/bg-13-6441-2016, 2016.

Lazzari, P., Solidoro, C., Ibello, V., Salon, S., Teruzzi, A., Béranger, K., Colella, S., and Crise, A.: Seasonal and inter-annual variability of plankton chlorophyll and primary production in the Mediterranean Sea: A modelling approach, Biogeosciences, 9, 217–233, https://doi.org/10.5194/bg-9-217-2012, 2012.

Lazzari, P., Salon, S., Terzić, E., Gregg, W. W., D'Ortenzio, F., Vellucci, V., Organelli, E., and Antoine, D.: Assessment of the spectral downward irradiance at the surface of the Mediterranean Sea using the radiative Ocean-Atmosphere Spectral Irradiance Model (OASIM), Ocean Science, 17, 675–697, https://doi.org/10.5194/os-17-675-2021, 2021a.

Lazzari, P., Álvarez, E., Terzić, E., Cossarini, G., Chernov, I., D'Ortenzio, F., and Organelli, E.: CDOM spatiotemporal variability in the Mediterranean Sea: a modelling study, J Mar Sci Eng, 9, 176-undefined, https://doi.org/10.3390/jmse9020176, 2021b.

Lazzari, P., Gharbi Dit Kacem, M., Álvarez, E., Chernov, I., and Vellucci, V.: Determination of biogeochemical properties in sea waters using the inversion of the three-stream irradiance model, Sci. Rep., 14, 22347, https://doi.org/10.1038/s41598-024-71457-5, 2024.

Lee, Z. P., Carder, K. L., and Arnone, R. A.: Deriving inherent optical properties from water color: a multiband quasi-analytical algorithm for optically deep waters, Appl. Opt., 41, 4957–4964, https://doi.org/10.1364/AO.41.005755, 2002.

Macé, L., Vandenbulcke, L., Brankart, J.-M., Brasseur, P., and Grégoire, M.: Characterisation of uncertainties in an ocean radiative transfer model for the Black Sea through ensemble simulations, Biogeosciences, 22, 3747–3768, https://doi.org/10.5194/bg-22-3747-2025, 2025.

Martinez-Vicente, V., Tilstone, G., Sathyendranath, S., Miller, P., and Groom, S.: Contributions of phytoplankton and bacteria to the optical backscattering coefficient over the Mid-Atlantic Ridge, Mar. Ecol. Prog. Ser., 445, 37–51, https://doi.org/10.3354/meps09388, 2012.

Mélin, F. and Vantrepotte, V.: How optically diverse is the coastal ocean?, Remote Sens Environ, 160, 235–251, https://doi.org/10.1016/j.rse.2015.01.023, 2015.

https://doi.org/10.5194/egusphere-2026-6687
Preprint. Discussion started: 5 November 2026
© Author(s) 2026. CC BY 4.0 License.

Menden-Deuer, S. and Lessard, E. J.: Carbon to volume relationships for dinoflagellates, diatoms and other protist plankton, Limnol Oceanogr, 45, 569–579, 2000.

Morel, A.: Optical properties of pure water and pure sea water, in: Optical Aspects of Oceanography, edited by: Jerlov, N. G. and Nielson, E. S., Academic Press, New York, 1–24, 1974.

Morel, A.: Optical modeling of the upper ocean in relation to its biogenous matter content (Case I waters), J Geophys Res, 93, 10749–10768, https://doi.org/10.1029/JC093iC09p10749, 1988.

Morel, A. and Gentili, B.: The dissolved yellow substance and the shades of blue in the Mediterranean Sea, Biogeosciences, 6, 2625–2636, https://doi.org/10.5194/bg-6-2625-2009, 2009.

Morel, A. and Prieur, L.: Analysis of variations in ocean color, Limnol Oceanogr, 22, 709–722, https://doi.org/10.4319/lo.1977.22.4.0709, 1977.

O'Reilly, J. E., Maritorena, S., Mitchell, B. G., Siegel, D. A., Carder, K. L., Garver, S. A., Kahru, M., and McClain, C.: Ocean color chlorophyll algorithms for SeaWiFS, J. Geophys. Res. Oceans, 103, 24937–24953, https://doi.org/10.1029/98JC02160, 1998.

Organelli, E., Bricaud, A., Antoine, D., and Matsuoka, A.: Seasonal dynamics of light absorption by chromophoric dissolved organic matter (CDOM) in the NW Mediterranean Sea (BOUSSOLE site), Deep-Sea Res Pt I, 91, https://doi.org/10.1016/j.dsr.2014.05.003, 2014.

Organelli, E., Dall'Olmo, G., Brewin, R. J. W., Tarran, G. A., Boss, E., and Bricaud, A.: The open-ocean missing backscattering is in the structural complexity of particles, Nat. Commun., 9, 5439, https://doi.org/10.1038/s41467-018-07814-6, 2018.

Pérez, G. L., Galí, M., Royer, S.-J., Sarmento, H., Gasol, J. M., Marrasé, C., and Simó, R.: Bio-optical characterization of offshore NW Mediterranean waters: CDOM contribution to the absorption budget and diffuse attenuation of downwelling irradiance, Deep-Sea Res Pt I, 114, 111–127, https://doi.org/10.1016/j.dsr.2016.05.011, 2016.

Pitarch, J., Bellacicco, M., Organelli, E., Volpe, G., Colella, S., Vellucci, V., and Marullo, S.: Retrieval of Particulate Backscattering Using Field and Satellite Radiometry: Assessment of the QAA Algorithm, Remote Sens. (Basel)., 12, 77, https://doi.org/10.3390/rs12010077, 2019.

Pujo-Pay, M., Conan, P., Oriol, L., Cornet-Barthaux, V., Falco, C., Ghiglione, J.-F., Goyet, C., Moutin, T., and Prieur, L.: Integrated survey of elemental stoichiometry (C, N, P) from the western to eastern Mediterranean Sea, Biogeosciences, 8, 883–899, https://doi.org/10.5194/bg-8-883-2011, 2011.

Ras, J., Claustre, H., and Uitz, J.: Spatial variability of phytoplankton pigment distributions in the Subtropical South Pacific Ocean: comparison between *in situ* and predicted data, Biogeosciences, 5, 353–369, https://doi.org/10.5194/bg-5-353-2008, 2008.

https://doi.org/10.5194/egusphere-2026-6687
Preprint. Discussion started: 5 November 2026
© Author(s) 2026. CC BY 4.0 License.

Saltelli, A., Ratto, M., Andres, T., Campolongo, F., Cariboni, J., Gatelli, D., Saisana, M., and Tarantola, S.: Global Sensitivity Analysis. The Primer, John Wiley & Sons, Ltd, Chichester, UK, https://doi.org/10.1002/9780470725184, 2007.

Serra-Pompei, C., Hickman, A., Britten, G. L., and Dutkiewicz, S.: Assessing the Potential of Backscattering as a Proxy for Phytoplankton Carbon Biomass, Global Biogeochem. Cycles, 37, https://doi.org/10.1029/2022GB007556, 2023.

Soto López, C. E., Gharbi Dit Kacem, M., Anselmi, F., and Lazzari, P.: Data-Informed Inversion Model (DIIM): a framework to retrieve marine optical constituents using a three-stream irradiance model, Geosci. Model Dev., 18, 7575–7602, https://doi.org/10.5194/gmd-18-7575-2025, 2025.

Storn, R. and Price, K.: Differential Evolution – A Simple and Efficient Heuristic for global Optimization over Continuous Spaces, Journal of Global Optimization, 11, 341–359, https://doi.org/10.1023/A:1008202821328, 1997.

Stramski, D., Bricaud, A., and Morel, A.: Modeling the inherent optical properties of the ocean based on the detailed composition of the planktonic community, Appl. Opt., 40, 2929, https://doi.org/10.1364/AO.40.002929, 2001.

Stramski, D., Boss, E., Bogucki, D., and Voss, K. J.: The role of seawater constituents in light backscattering in the ocean, Prog. Oceanogr., 61, 27–56, https://doi.org/10.1016/j.pocean.2004.07.001, 2004.

Terzić, E., Miró, A., Organelli, E., Kowalczuk, P., D'Ortenzio, F., and Lazzari, P.: Radiative transfer modeling with Biogeochemical-Argo float data in the Mediterranean Sea, J Geophys Res-Oceans, 126, e2021JC01769, https://doi.org/10.1029/2021JC017690, 2021.

Usher, W., Herman, J., Whealton, C., Hadka, D., xantares, Rios, F., bernardoct, Mutel, C., and van Engelen, J.: SALib/SALib: Launch! , https://doi.org/https://doi.org/10.5281/zenodo.598306, 2016., 2016.

Utermöhl, H.: Zur Vervollkommnung der quantitativen Phytoplankton-Methodik, Mitt. Int. Ver. Theor. Angew. Limnol., 9, 1–38, 1958.

Vaillancourt, R. D., Brown, C. W., Guillard, R. R. L., and Balch, W. M.: Light backscattering properties of marine phytoplankton: relationships to cell size, chemical composition and taxonomy, J Plankton Res, 26, 191–212, 2004.

Vichi, M., Pinardi, N., and Masina, S.: A generalized model of pelagic biogeochemistry for the global ocean ecosystem. Part I: Theory, J Marine Syst, 64, 89–109, https://doi.org/10.1016/j.jmarsys.2006.03.006, 2007.

Vichi, M., Lovato, T., Butenschön, M., Tedesco, L., Lazzari, P., Cossarini, G., Masina, S., Pinardi, N., Solidoro, C., and Zavatarelli, M.: The Biogeochemical Flux Model (BFM): Equation Description and User Manual. BFM version 5.2. BFM Report series N. 1, Release 1.2, Bologna, http://bfm-community.eu (last access: 3 March 2023), 2020.

Volpe, G., Colella, S., Brando, V. E., Forneris, V., La Padula, F., Di Cicco, A., Sammartino, M., Bracaglia, M., Artuso, F., and Santoleri, R.: Mediterranean ocean colour Level 3 operational multi-sensor processing, Ocean Science, 15, 127–146, https://doi.org/10.5194/os-15-127-2019, 2019.

https://doi.org/10.5194/egusphere-2026-6687
Preprint. Discussion started: 5 November 2026
© Author(s) 2026. CC BY 4.0 License.

Westberry, T., Behrenfeld, M. J., Siegel, D. A., and Boss, E.: Carbon-based primary productivity modeling with vertically resolved photoacclimation, Global Biogeochem Cy, 22, GB2024, https://doi.org/10.1029/2007GB003078, 2008.

Wolanin, A., Soppa, M., and Bracher, A.: Investigation of Spectral Band Requirements for Improving Retrievals of Phytoplankton Functional Types, Remote Sens. (Basel)., 8, 871, https://doi.org/10.3390/rs8100871, 2016.

Woźniak, S. B., Sagan, S., Zabłocka, M., Stoń-Egiert, J., and Borzycka, K.: Light scattering and backscattering by particles suspended in the Baltic Sea in relation to the mass concentration of particles and the proportions of their organic and inorganic fractions, Journal of Marine Systems, 182, 79–96, https://doi.org/10.1016/j.jmarsys.2017.12.005, 2018.

Xing, X., Claustre, H., Wang, H., Poteau, A., and D'Ortenzio, F.: Seasonal dynamics in colored dissolved organic matter in the Mediterranean Sea: Patterns and drivers, Deep-Sea Res Pt I, 83, 93–101, https://doi.org/10.1016/j.dsr.2013.09.008, 2014.

Zaneveld, J. R. V.: A theoretical derivation of the dependence of the remotely sensed reflectance of the ocean on the inherent optical properties, J. Geophys. Res. Oceans, 100, 13135–13142, https://doi.org/10.1029/95JC00453, 1995.

Zeng, C., Zeng, T., Fischer, A., and Xu, H.: Fluorescence-Based Approach to Estimate the Chlorophyll-A Concentration of a Phytoplankton Bloom in Ardley Cove (Antarctica), Remote Sens. (Basel)., 9, 210, https://doi.org/10.3390/rs9030210, 2017.

Zibordi, G. and Berthon, J.-F.: Coastal Atmosphere & Sea Time Series (CoASTS) and Bio-Optical mapping of Marine optical Properties (BiOMaP): the near- surface marine bio-optical data [dataset], 2024., 2024.

Zibordi, G., Mélin, F., Berthon, J.-F., Holben, B., Slutsker, I., Giles, D., D'Alimonte, D., Vandemark, D., Feng, H., Schuster, G., Fabbri, B. E., Kaitala, S., and Seppälä, J.: AERONET-OC: A Network for the Validation of Ocean Color Primary Products, J. Atmos. Ocean. Technol., 26, 1634–1651, https://doi.org/10.1175/2009JTECHO654.1, 2009.

Zingone, A., Totti, C., Sarno, D., Cabrini, M., Caroppo, C., Giacobbe, M. G., Lugliè, A., Nuccio, C., and Socal, G.: Fitoplancton: metodiche di analisi quali-quantitativa, in: Metodologie di studio del plancton marino, edited by: Socal, G., Buttino, I., Cabrini, M., Mangoi, O., Penna, A., and Totti, C., Manuali e Linee Guida 56/200 ISPRA, SIBM, Roma, 213–237, 2010.